



Theses and Dissertations

2003-05-14

Azimuth Modulation of the Radar Backscatter at Near-Normal Incidence

Andrew D. Greenwood
Brigham Young University - Provo

Follow this and additional works at: <https://scholarsarchive.byu.edu/etd>



Part of the [Electrical and Computer Engineering Commons](#)

BYU ScholarsArchive Citation

Greenwood, Andrew D., "Azimuth Modulation of the Radar Backscatter at Near-Normal Incidence" (2003). *Theses and Dissertations*. 70.

<https://scholarsarchive.byu.edu/etd/70>

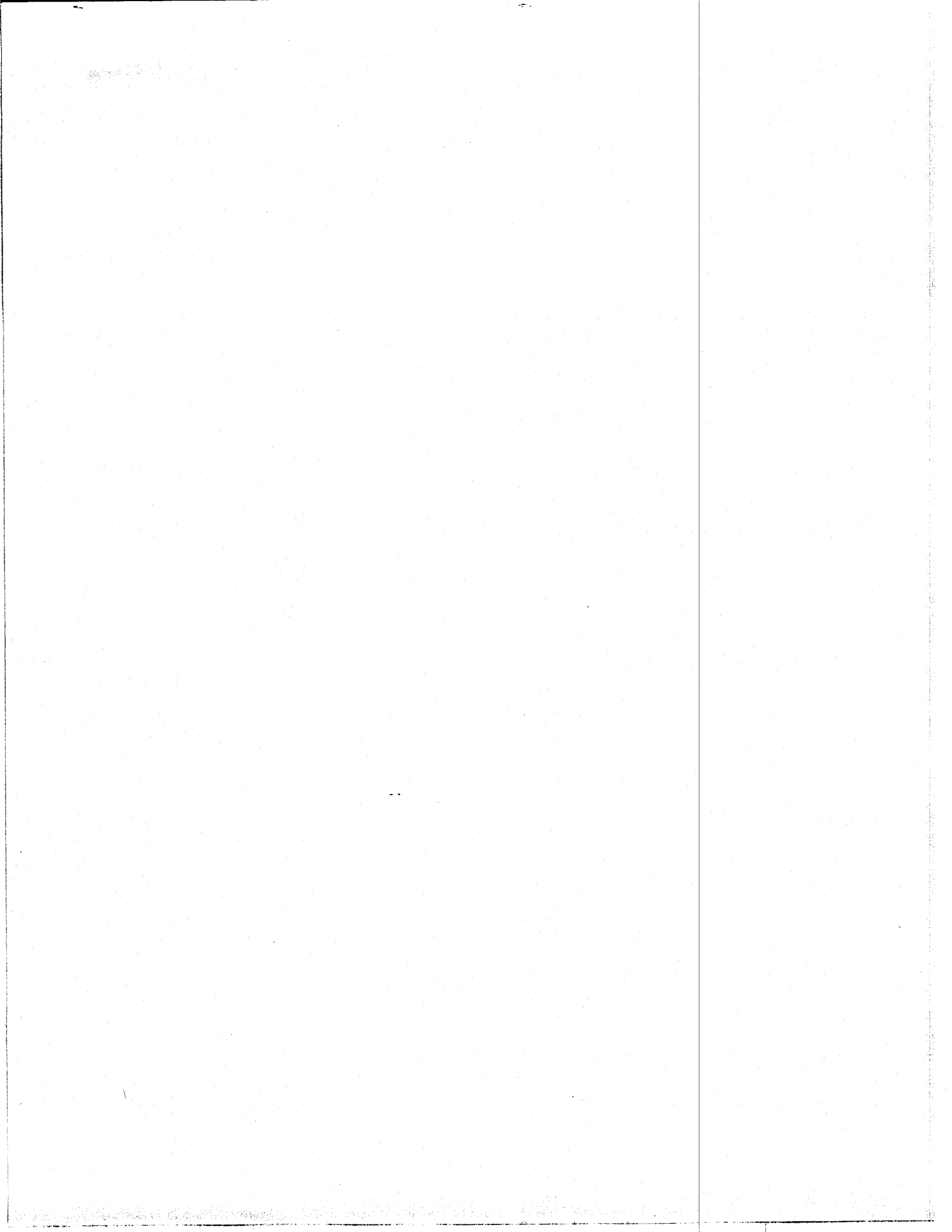
This Thesis is brought to you for free and open access by BYU ScholarsArchive. It has been accepted for inclusion in Theses and Dissertations by an authorized administrator of BYU ScholarsArchive. For more information, please contact scholarsarchive@byu.edu, ellen_amatangelo@byu.edu.

AZIMUTH MODULATION OF THE RADAR
BACKSCATTER AT NEAR-NORMAL
INCIDENCE

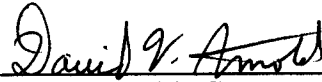
A Thesis
Submitted to the
Department of Electrical and Computer Engineering
Brigham Young University

In Partial Fulfillment
of the Requirements for the Degree
Master of Science

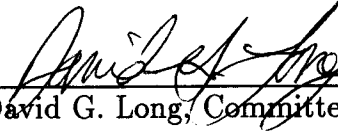
by
Andrew D. Greenwood
June 7, 1995



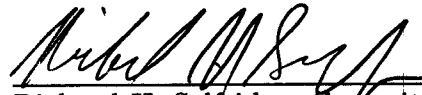
This thesis by Andrew D. Greenwood is accepted in its present form by the Department of Electrical and Computer Engineering of Brigham Young University as satisfying the thesis requirement for the degree of Master of Science.



David V. Arnold, Committee Chairman



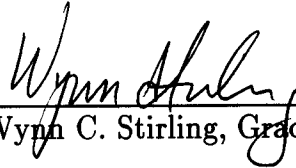
David G. Long, Committee Member



Richard H. Selfridge, Committee Member

JUNE 9, 1995

Date



Wynn C. Stirling, Graduate Coordinator

ACKNOWLEDGMENTS

There are many individuals whose assistance has been made this work possible. Dr. David Arnold, who has served as my thesis advisor, has provided able and willing help on a number of questions that have arisen, and has encouraged me to pursue new and challenging goals. Dr. David Long, who has served on my thesis committee, has also provided able and willing assistance and helped me to identify a fellowship as a funding source. Paul Johnson, a fellow graduate student, who studied similar scattering problems at normal incidence has assisted numerous times as well. Thanks are also due to Ryan Reed, who provided radar data from the YSCAT system, and to Scott Collyer, who created some of the data processing routines used to extract the YSCAT data.

Personally, I must also thank my wife, Cheryl, who has been patient and encouraging throughout this work, and has been willing to tolerate some late nights in the laboratory. Finally, my parents, Doug and Marcia, have encouraged me to be the best I can be throughout my life. Thanks to all of you. I could not have done it without your help.

Contents

Acknowledgments	iii
1 Introduction	1
1.1 Overview	1
1.2 Contributions	3
2 Theoretical Scattering at Near-Normal Incidence	4
2.1 The Surface Model	4
2.1.1 Qualitative surface description	5
2.1.2 The correlation coefficient	7
2.2 Derivation of the Normalized Radar Cross-Section	11
2.3 Evaluation of the Backscatter Integral	17
2.3.1 Numerical evaluation	18
2.3.2 Asymptotic evaluation	19
2.4 Summary	27
3 Theoretical Azimuth Modulation at Near-Normal Incidence	28
3.1 Physical Discussion	28
3.1.1 Scattering from a flat surface versus a rough surface	28
3.1.2 Scattering from a unidirectional surface	30
3.1.3 Scattering from a random, rough surface	30
3.2 Sensitivity of Azimuth Modulation to Model Parameters	31
3.2.1 Dependence on the power parameter (p)	33
3.2.2 Dependence on the low wave number cut-off (k_0)	33
3.2.3 Dependence on the directional parameter (θ_0)	36
3.2.4 Dependence on the incidence angle (θ_i)	37
3.2.5 Dependence on the radar frequency (f)	37
3.3 Summary	37
4 Experimental Azimuth Modulation at Near-Normal Incidence	42
4.1 Data Collection	42
4.1.1 The YSCAT radar system	44
4.1.2 YSCAT data collection at near-normal incidence	45
4.1.3 Other experimental sensors	46
4.2 Known Measurement Errors	47
4.2.1 Azimuth slip	47
4.2.2 Clock drift	47
4.3 Comparison of Experimental Results to Theory.	48
4.3.1 General data processing	50

4.3.2	Relative normalized radar cross-section vs. azimuth angle . .	51
4.3.3	Modulation magnitude vs. roughness	54
4.4	Summary	57
5	Conclusions	59
5.1	Contributions	59
5.2	Extensions	61
A	Derivation of Correlation Coefficient	65
B	Derivation of Backscatter Assuming Horizontal Polarization	70
C	Mean and Fluctuating Fields	72

List of Tables

2.1	Definition of symbols used in the surface model derivation	6
2.2	Definition of symbols used in the backscatter derivation	14

List of Figures

2.1	Geometry of the system.	5
2.2	Dependence of the power spectral density on wave number.	8
2.3	Functions describing the directionality of the power spectral density	9
2.4	Effects of the surface parameters on the correlation coefficient. . . .	12
2.5	Effect of azimuth angle on the correlation coefficient.	13
2.6	Results of modified Romberg integration	19
2.7	Asymptotic expansions for $p < 4$	23
2.8	Asymptotic expansions for $p > 4$	26
3.1	Results of modified Romberg integration	29
3.2	Scattering from a perfectly flat surface ($\sigma = 0$).	30
3.3	Scattering from a unidirectional surface.	31
3.4	Scattering from rough surfaces.	32
3.5	Dependence of the modulation on the power parameter (p).	34
3.6	Dependence of the modulation on the low wave number cut-off (k_0).	35
3.7	Dependence of the modulation on the directional parameter (θ_0).	36
3.8	Dependence of the modulation on incidence angle (θ_i).	38
3.9	Scattering from a rough surface at two incidence angles.	39
3.10	Dependence of the modulation on the radar frequency (f).	40
4.1	Map showing the location of the CCIW Research Tower.	43
4.2	Diagram of YSCAT deployment on the CCIW Tower.	44
4.3	Photo of YSCAT deployment on CCIW research tower.	45
4.4	Empirical results from data gathered at the YSCAT experiment.	49
4.5	Relative σ° (small surface roughness): comparison of measured values to theoretical values.	52
4.6	Relative σ° (large surface roughness): comparison of measured values to theoretical values	53
4.7	Comparison of measured values of the modulation magnitude to theoretical values as a function of surface roughness.	56
4.8	Ratio of modulation magnitude at 20° to modulation magnitude at 10°	57
C.1	Fluctuating backscatter compared to total backscatter.	74

INTRODUCTION

Radar observations of the ocean surface are becoming increasingly important. Common applications are wind retrieval and global weather forecasting and characterization. Because of the common use of ocean radar measurements, it is important to understand the scattering characteristics of rough, ocean surfaces. In particular, it is important to understand the sensitivity of the backscatter to both radar parameters and surface parameters.

At near-normal incidence angles, it has been assumed that the radar backscatter exhibits little or no azimuth dependence (Colton, 1989). However, recent data taken by the BYU YSCAT radar system suggests that this is not the case. At an incidence angle of 10° , the YSCAT radar data shows from a fraction of a decibel to up to 10 decibels of azimuth modulation, depending on the surface conditions. In this thesis, a physical optics approach is used with a two-dimensional surface model to derive the electromagnetic backscatter from the ocean surface. If the waves on the ocean surface are directed, azimuth modulation is predicted at near-normal incidence angles. The effects of surface and radar parameters on the azimuth modulation are studied, and the results are compared to data taken by the YSCAT radar system. It is shown that the theory correctly predicts of the shape of the curve when the normalized radar cross-section is plotted as a function of azimuth angle. The theory also predicts the correct trend of the modulation magnitude as a function the surface roughness. However, the simplifications in the model limit its prediction of the frequency dependence of the modulation. Relaxing some of the assumptions of the model is likely to correct this problem.

1.1 Overview

The first step in predicting the azimuth modulation is to characterize the ocean surface. The surface is modeled as a two-dimensional stochastic process which is assumed to have Gaussian statistics. The process is assumed zero-mean

and wide-sense stationary. The power spectral density is modeled as a function of wavenumber and wave direction. The wavenumber dependence is described by k_w^{-p} for k_w larger than the low wavenumber cut-off, k_0 , and the directional dependence is described by a Gaussian function whose width is varied with the directional parameter, θ_0 . The correlation coefficient, which is needed to derive the radar backscatter, is found by evaluating the inverse Fourier transform of the power spectral density.

After characterizing the ocean surface, the backscatter is found using Green's theorem and the tangent plane approximation. The result is an integral expression that is referred to as the backscatter integral. Asymptotic approximation and numerical integration are used to evaluate the integral, which is the basis for predicting the azimuth modulation.

After finding the expected backscatter, the physical reasons for azimuth modulation are discussed. A directed surface leads to azimuth modulation, and the amount of modulation depends on the orientation of surface facets in different azimuth directions. For practical ocean surfaces, the azimuth modulation is predicted to decrease as the surface becomes increasingly rough. In general, the modulation also depends on the surface parameters and the radar parameters. The surface parameters effect the orientation of the surface facets, and the radar parameters effect which surface facets produce backscatter. Thus, any of these parameters can effect the azimuth modulation.

Once the theory has been established, it is compared to radar data. First, the YSCAT94 radar experiment is described. Methods of data collection are discussed, and known data errors are corrected. The data is then compared to the theory. The theory predicts a curve similar to a cosine wave when the normalized radar cross-section is plotted as a function of azimuth angle. As mentioned above, it is shown that this prediction is the correct shape of the modulation curve. The radar data also exhibits decreasing azimuth modulation as the surface becomes increasingly rough, as predicted by the theory. However, the theory predicts that the modulation will remain constant as the radar frequency is varied. In the data, the modulation is increasing as the radar frequency is increased. The prediction of this frequency trend has been limited by assumptions in the surface model. The

correct frequency trend is likely to be predicted if the assumptions on the power spectrum of the surface are relaxed.

1.2 Contributions

While azimuth modulation has been observed incidence angles larger than 20° , little understanding has been developed for near normal incidence angles ($< 20^\circ$). In fact, many have assumed that no modulation is present at near-normal incidence. This work shows that modulation is present at near-normal incidence angles. Further, it develops a theory which predicts the shape of the modulation curve and the dependence of the modulation on surface roughness. It is a step toward improved understanding of azimuth modulation of the radar backscatter.

THEORETICAL SCATTERING AT NEAR-NORMAL INCIDENCE

This chapter considers the derivation of an expression for the electromagnetic backscatter from a rough, ocean surface. In order to derive the backscatter, a descriptive model of the surface is first needed. Due to the complexity of the ocean surface, the most useful models are statistical; thus, the surface is modeled as a stochastic process. It is assumed that the statistics of the surface are Gaussian and wide-sense stationary over distances on the order of the size of a typical radar footprint. Under the stated assumptions, knowledge of the mean, variance, and correlation of the stochastic process are all that are necessary to characterize the surface. In particular, values of the correlation coefficient are needed to find the backscatter. Thus, much of the section on the surface is devoted to describing its correlation.

Once the surface has been described, the backscatter can be found using Physical Optics and Green's theorem. The tangent plane approximation is used in connection with the surface model to find the source current term for Green's theorem. The result of the derivation is an integral expression for the normalized radar cross section. This integral is referred to as the backscatter integral. Methods of evaluating or approximating the backscatter integral include numerical integration and asymptotic evaluation.

2.1 The Surface Model

Before attempting to describe the ocean surface, it is first necessary to define a coordinate system as a frame of reference. The coordinate system is shown in Figure 2.1. Figure 2.1a shows that the radar antenna is located in the x - z plane and that θ_i represents the radar incidence angle. Similarly, Figure 2.1b shows that the coordinate origin is the center of radar footprint, and the mean of the surface height is the $x - y$ plane. The radar footprint is assumed to be $L \times L$ in size, and

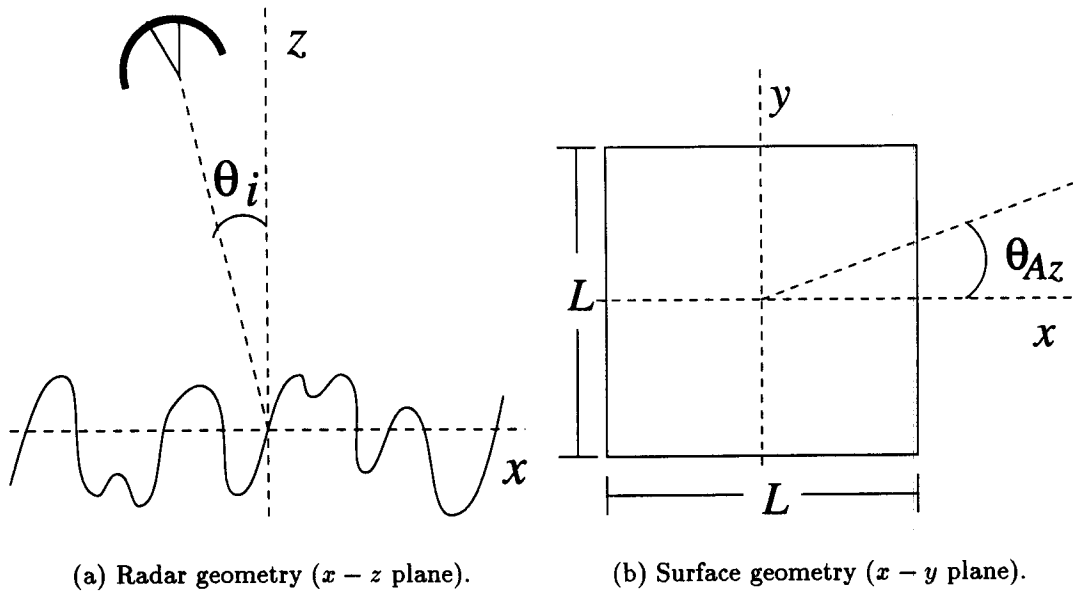


Figure 2.1: Geometry of the system. The radar antenna is located in the $x - z$ plane, and the mean of the surface height is defined to be the $x - y$ plane.

θ_{Az} is the relative azimuth angle, the angle between the x -axis and the dominant wave direction on the surface. (Recall that the x -axis is defined by the location of the radar antenna.) For reference, all of the symbols used in the surface description are summarized in Table 2.1.

2.1.1 Qualitative surface description

The development of a precise description of the ocean surface is a very complex problem. As previously mentioned, the most useful approach is to model the ocean surface as a two-dimensional stochastic process. Thus the height of the surface at each point is represented by a random variable, $\eta(x, y)$. It is assumed that the statistics of the surface are Gaussian. Under the assumption that the ocean statistics are Gaussian, knowledge of the surface mean, variance, and correlation coefficient are necessary to characterize the surface.

It is assumed that the surface is wide sense stationary over distances on the order of the size of the radar footprint. Under this assumption, the surface mean and variance are constants, and the correlation coefficient is a function only

Symbol	Explanation
(x, y, z)	Rectangular coordinates of a point on the surface
(ρ, ϕ, z)	Cylindrical coordinates of a point on the surface
$\eta(x', y')$	Height of the ocean surface at point (x', y')
L	Dimension of radar footprint
σ	Standard deviation of the ocean surface height
k_w	Wave number on the ocean surface
p	Power parameter of the surface
k_0	Spectral peak on the surface
θ	Wave direction on the ocean surface
θ_{Az}	Angle between the x-axis and the dominant wave direction (see Figure 2.1)
$P(k_w, \theta)$	Power spectral density of the ocean surface height process
$W(\theta)$	Function describing the dependence of the power spectral density on wave direction
S_0	Normalization constant in the power spectral density function
$C_p(x, y)$	Correlation Coefficient of the ocean surface (distances in rectangular coordinates)
$C_p(\rho, \phi)$	Correlation Coefficient of the ocean surface (distances in polar [cylindrical] coordinates)
γ	Euler-Mascheroni constant (0.577215664901...)

Table 2.1: Definition of symbols used in the surface model derivation

of the x-distance and the y-distance between two surface points. The coordinate system (see Figure 2.1) is defined such that the surface mean is zero. The surface variance is represented by σ^2 , and the surface correlation coefficient is denoted $C_p(x, y)$ in rectangular coordinates or $C_p(\rho, \phi)$ in polar coordinates.

2.1.2 The correlation coefficient

To find the surface correlation coefficient, first consider the power spectral density of the waves on the surface. The power spectral density is a function of the wave number k_w and the wave direction θ , and it is denoted $P(k_w, \theta)$. The correlation coefficient and the power spectral density form a Fourier transform pair. The dependence of the power spectral density on the wave number is assumed to follow the model $P(k_w) = k_w^{-p} u(k_w - k_0)$ where $u(\cdot)$ represents the unit step function (Phillips, 1966, pp. 111-113, Donelan and Pierson, 1987). This function is linear in log-log space. For two dimensional surfaces, the power parameter (p), has been empirically shown to lie in the range $3 < p < 5$ (Banner et al., 1989, Jahne and Riemer, 1990, Shemdin et al., 1988). This model for the power spectral density has been simplified from that plotted by Phillips in that a sharp cut-off is assumed at $k = k_w$ rather than a function that tapers to zero (see Figure 2.2). This sharp cut-off causes the correlation coefficient (the inverse Fourier transform of the power spectral density) to oscillate with a behavior similar to $\frac{\sin x}{x}$. This infinite oscillation is tolerable, however, because the correlation is of interest only for points a small distance apart.

The k_w^{-p} model for the power spectral density is valid only for some segment of wave numbers in the spectrum. The low wave number cut-off, k_0 , is defined to be the peak of the spectrum in the region of interest. For the purposes of this derivation, the region of interest corresponds to the part of the spectrum that is known to dominate the backscatter. Typically, this region contains those waves whose height is on the order of one electromagnetic wavelength. An upper wave number cut-off for the region of interest is not needed for the model because the physical optics approach contains an implicit surface filtering function (Arnold, 1992).

The power spectral density dependence on the wave direction is not

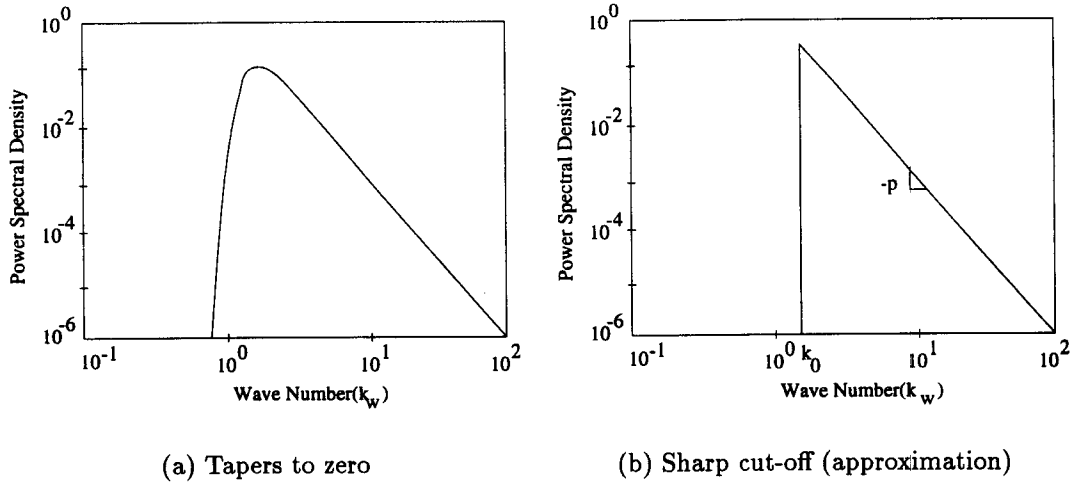


Figure 2.2: Dependence of the power spectral density on wave number. Figure a is a sketch similar to plots by Phillips (Phillips, 1966, p. 113). Figure b shows the approximation using a sharp cut-off.

well understood, although it is reasonable to believe that waves do not propagate equally in all directions. In fact, ocean waves are wind driven, and most of the wave energy propagates in directions close to that of the wind. A function of the form

$$h(\theta) = \cos^q\left(\frac{\theta - \theta_{Az}}{2}\right) \quad (2.1)$$

has been used to describe the directional dependence of the power spectral density (Donelan et al., 1983). Plots of $h(\theta)$ (normalized by its area) for various values of q are shown in Figure 2.3a. While $h(\theta)$ is consistent with the expected directional properties of wind driven waves, it is difficult to work with under integration. Thus, the directional dependence of the power spectrum is assumed to be of the form

$$W(\theta) = \exp\left[-3\left(\frac{\theta - \theta_{Az}}{\theta_0}\right)^2\right], \quad \theta_{Az} - \frac{\pi}{2} \leq \theta \leq \theta_{Az} + \frac{\pi}{2}. \quad (2.2)$$

where θ_0 is a parameter describing the width of the directivity. Plots of $W(\theta)$ (normalized by its area) for various values of θ_0 are shown in Figure 2.3b. The function $W(\theta)$ is chosen instead of $h(\theta)$ because the two functions differ little in shape and in value, and $W(\theta)$ is easier to work with under integration. Because of the assumption that the statistics of the surface are Gaussian, there is a 180°

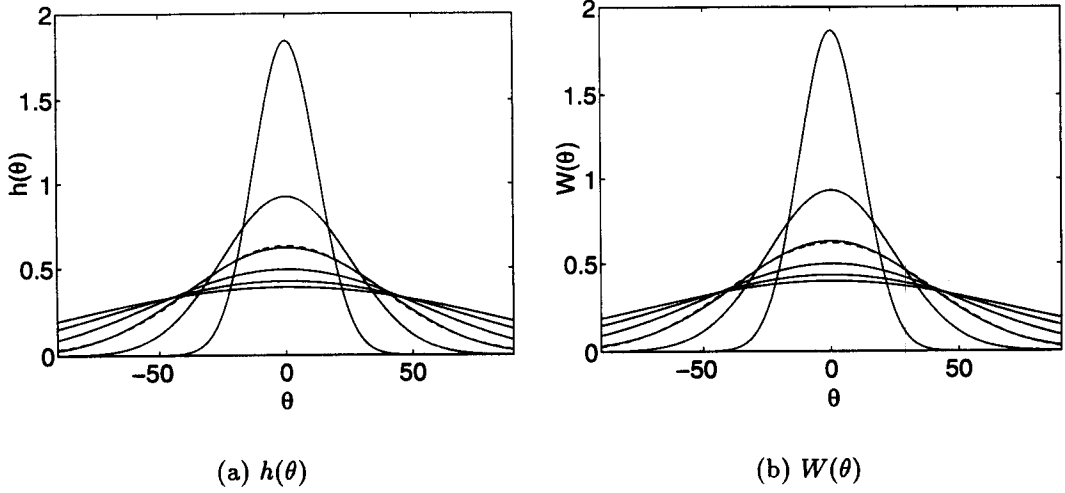


Figure 2.3: Functions describing the directionality of the power spectral density. Figure a shows $h(\theta)$ (normalized for by its area) for $q = 85, 21, 9, 5, 3,$ and 2 . Figure b shows $W(\theta)$ (normalized by its area) for $\theta_0 = 30^\circ, 60^\circ, 90^\circ, 120^\circ, 150^\circ,$ and 180° . For comparison, $W(\theta)$ for $\theta_0 = 90^\circ$ is shown (dotted line) on the $h(\theta)$ plot, and $h(\theta)$ for $q = 9$ is shown (dotted line) on the $W(\theta)$ plot. In this thesis, $W(\theta)$ is used to describe the surface directionality.

ambiguity in the direction of wave propagation. Hence, if θ is outside of the range $\theta_{Az} - \frac{\pi}{2} \leq \theta \leq \theta_{Az} + \frac{\pi}{2}$, the value of $W(\theta)$ is found by symmetry.

As mentioned, the directivity of the surface is described by θ_0 in $W(\theta)$. If θ_0 is very small, the waves are almost unidirectional, and the surface is highly directed. For $\theta_0 \approx \pi$, the waves are traveling in all directions, and the surface is nearly isotropic. $W(\theta)$ has been defined such that its half-power points are located at $\theta = \theta_{Az} \pm \frac{\theta_0}{2}$.

Putting the wavenumber and directionality pieces together, the complete power spectral density is given by

$$P(k_w, \theta) = S_0 k_w^{-p} u(k_w - k_0) \exp \left[-3 \left(\frac{\theta - \theta_{Az}}{\theta_0} \right)^2 \right], \quad \theta_{Az} - \frac{\pi}{2} \leq \theta \leq \theta_{Az} + \frac{\pi}{2} \quad (2.3)$$

where S_0 is a normalization constant to be evaluated below.

The correlation coefficient of the surface can now be found by evaluating the inverse Fourier transform of Equation 2.3. To facilitate the derivation, the correlation coefficient is represented as a function of polar coordinates (ρ and ϕ)

instead of rectangular coordinates (x and y). After simplifying the Fourier integral using symmetry arguments, the correlation coefficient is given by

$$C_p(\rho, \phi) = S_0 \int_{\theta_{Az}-\frac{\pi}{2}}^{\theta_{Az}+\frac{\pi}{2}} d\theta \exp \left[-3 \left(\frac{\theta - \theta_{Az}}{\theta_0} \right)^2 \right] \int_{k_0}^{\infty} dk_w k_w^{-p+1} \cos(k_w \rho |\cos(\theta - \phi)|). \quad (2.4)$$

S_0 , the normalization constant, can be determined by setting $\rho = 0$, evaluating the integral, and noting that $C_p(0, 0) = 1$. Thus,

$$S_0 = \frac{(p-2)k_0^{p-2}}{\frac{\pi}{3}\theta_0 \operatorname{erf}\left(\frac{\sqrt{3}\pi}{2\theta_0}\right)}. \quad (2.5)$$

Unfortunately, the integral for $C_p(\rho, \phi)$ has no closed form result for general ρ and ϕ . It is, however, possible to find a series solution for the inner (dk_w integral) when p is not an integer. The details of the series derivation are presented in Appendix A. Applying the series result yields

$$C_p(\rho, \phi) = 1 + \frac{(p-2)}{\frac{\pi}{3}\theta_0 \operatorname{erf}\left(\frac{\sqrt{3}\pi}{2\theta_0}\right)} \cos \left[\frac{\pi}{2}(p-2) \right] \Gamma(2-p)(k_0\rho)^{p-2} I_1(p-2, \phi) - \frac{(p-2)}{\frac{\pi}{3}\theta_0 \operatorname{erf}\left(\frac{\sqrt{3}\pi}{2\theta_0}\right)} \sum_{r=1}^{\infty} \frac{(-1)^r (k_0\rho)^{2r}}{(2r)!(2-p+2r)} I_1(2r, \phi) \quad (2.6)$$

where

$$I_1(\nu, \phi) = \int_{\theta_{Az}-\frac{\pi}{2}}^{\theta_{Az}+\frac{\pi}{2}} d\theta |\cos(\theta - \phi)|^\nu \exp \left[-3 \left(\frac{\theta - \theta_{Az}}{\theta_0} \right)^2 \right]. \quad (2.7)$$

Upon inspection, it can be seen that Equation 2.6 is singular for integer p . Since $3 < p < 5$, $p = 4$ is the only integer value of concern. In Appendix A, an alternate series is derived for the case $p = 4$, resulting in

$$C_4(\rho, \phi) = 1 + \frac{(k_0\rho)^2}{\frac{\pi}{3}\theta_0 \operatorname{erf}\left(\frac{\sqrt{3}\pi}{2\theta_0}\right)} I_2(\rho, \phi) + \left(\gamma - \frac{3}{2}\right) \frac{(k_0\rho)^2}{\frac{\pi}{3}\theta_0 \operatorname{erf}\left(\frac{\sqrt{3}\pi}{2\theta_0}\right)} I_1(2, \phi) - \frac{1}{\frac{\pi}{3}\theta_0 \operatorname{erf}\left(\frac{\sqrt{3}\pi}{2\theta_0}\right)} \sum_{r=2}^{\infty} \frac{(-1)^r (k_0\rho)^{2r}}{(2r-2)(2r)!} I_1(2r, \phi) \quad (2.8)$$

where γ is the Euler-Mascheroni constant, $I_1(\nu, \phi)$ is given by Equation 2.7, and $I_2(\rho, \phi)$ is given by

$$I_2(\rho, \phi) = \int_{\theta_{Az}-\frac{\pi}{2}}^{\theta_{Az}+\frac{\pi}{2}} d\theta \cos^2(\theta - \phi) \ln(k_0\rho |\cos[\theta - \phi]|) \exp \left[-3 \left(\frac{\theta - \theta_{Az}}{\theta_0} \right)^2 \right]. \quad (2.9)$$

Plots of the correlation coefficient are shown in Figures 2.4 and 2.5. Figure 2.4 also shows the effect of the various surface parameters on the correlation coefficient. Changing p causes the function to fall off faster or slower near the origin; changing k_0 stretches or shrinks the function with respect to the x and y axes, and changing θ_0 makes the function appear more rounded or more oblong. Figure 2.5 shows that changing the radar azimuth angle (θ_{Az}) rotates the function about the z -axis.

The mean, variance, and correlation coefficient of the surface have now been found. Because the statistics of the surface are assumed to be Gaussian and wide-sense stationary over the area of the radar footprint, the surface has been completely characterized. In summary, the ocean surface is modeled as a two-dimensional Gaussian random process. The mean of the process is zero, and the variance is σ^2 . The correlation coefficient is found by first considering the power spectral density, which is given by Equation 2.3 where $3 < p < 5$. If $p \neq 4$, the correlation coefficient is then given by Equation 2.6. When $p = 4$, the correlation coefficient is given by Equation 2.8.

2.2 Derivation of the Normalized Radar Cross-Section

After developing a description of the ocean surface, that description can be used to derive the expected radar backscatter from the surface. The geometry of the system is the same as that used to derive the surface description and is shown in Figure 2.1. It is assumed that the ocean surface is in the far field of the radar antenna and that all electromagnetic fields are time harmonic. For this derivation, it is also assumed that the radar is transmitting a vertically polarized electric field (v-pol). A parallel derivation is given in Appendix B assuming a horizontally polarized electric field. Because the tangent plane approximation is used in the derivation, any backscatter dependence on the polarization is lost. Hence, both derivations result in an identical expression for the normalized radar cross section (σ°).

The development is an extension of that given by Johnson (Johnson, 1994). Johnson considered only normal incidence; here, small off-normal incident angles are considered. Because shadowing and multiple scattering are ignored, the incidence angle must be limited to less than approximately 20° .

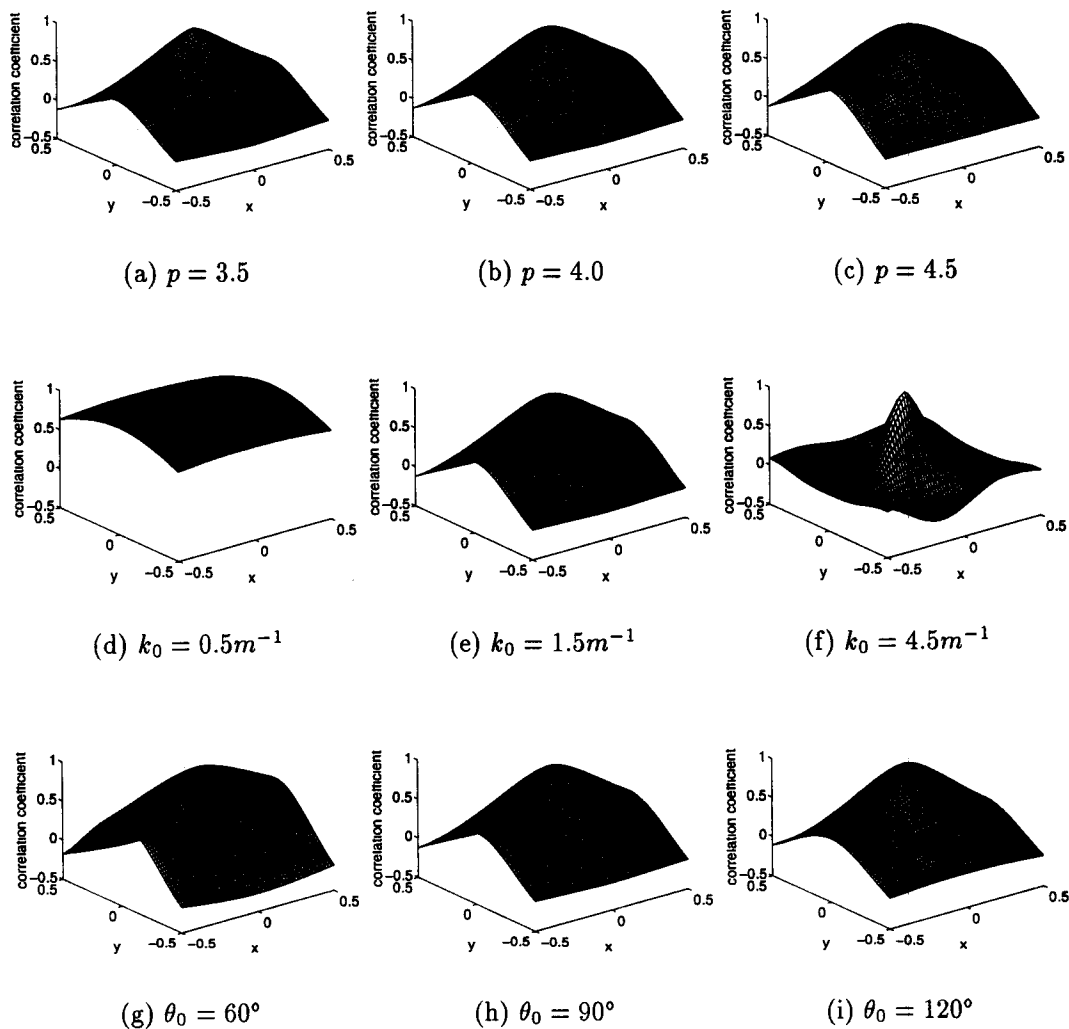


Figure 2.4: Effects of the surface parameters on the correlation coefficient. Unless otherwise specified, $p = 4.0$, $k_0 = 1.5m^{-1}$, and $\theta_0 = 90^\circ$. Changing p causes the function to fall off faster or slower near the origin; changing k_0 stretches or shrinks the function with respect to the x and y axes, and changing θ_0 makes the function appear more rounded or more oblong.

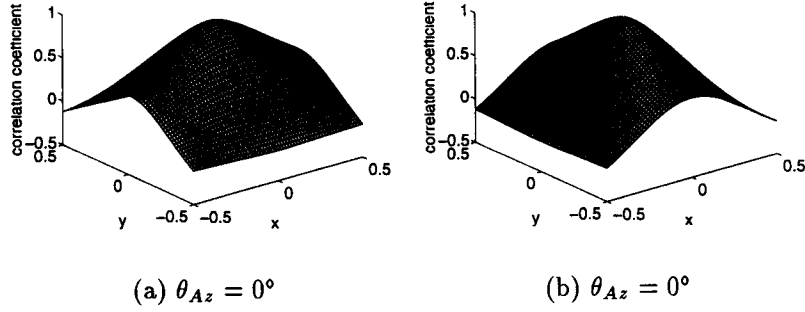


Figure 2.5: The effect of the azimuth angle on the correlation coefficient is to rotate the function about the z -axis. The surface parameters are $p = 4.0$, $k_0 = 1.5m^{-1}$, and $\theta_0 = 90^\circ$.

At microwave frequencies, the ocean is modeled as a nearly perfect conductor. When microwave radiation strikes the surface, a surface current is induced. This surface current then generates a reflected wave according to Green's theorem. Thus, the approach to derive the backscatter is to find the current induced on the surface by the incident (transmitted) field, and then apply Green's theorem. The induced current becomes the source term in Green's theorem.

Green's theorem states that

$$\vec{E}_s(\vec{r}) = i\omega\mu_0 \int_{V'} dV' \overline{\overline{G}}(\vec{r}, \vec{r}') \cdot \vec{J}(\vec{r}') \quad (2.10)$$

where $\overline{\overline{G}}(\vec{r}, \vec{r}')$ is the dyadic Green's function and $\vec{J}(\vec{r}')$ is the source current density (Kong, 1990m p. 230). The symbols used in the backscatter derivation are summarized in Table 2.2 to avoid any ambiguity.

In three dimensions, the dyadic Green's function is given by

$$\overline{\overline{G}}(\vec{r}, \vec{r}') = (\overline{\overline{I}} + \frac{1}{k^2} \nabla \nabla) g(\vec{r}, \vec{r}') \quad (2.11)$$

where $g(\vec{r}, \vec{r}')$ is the scalar Green's function. The scalar Green's function is in turn given by

$$g(\vec{r}, \vec{r}') = \frac{e^{ik|\vec{r}-\vec{r}'|}}{4\pi|\vec{r}-\vec{r}'|}. \quad (2.12)$$

The Green's function can be simplified based on the geometry and conditions of the problem. Recall that the ocean surface is in the far field of the radar

Symbol	Explanation
\vec{r}	Coordinates of observation point (radar antenna)
\vec{r}'	Coordinates of source point (on surface)
$\hat{r}, \hat{\theta}, \hat{\phi}$	Unit vectors in spherical coordinate system
$\hat{x}, \hat{y}, \hat{z}$	Unit vectors in rectangular coordinate system
(x, y, z)	Rectangular coordinates of an observation point (radar antenna)
(x', y', z')	Rectangular coordinates of a point in the source region (on the surface)
\hat{n}	Unit vector normal to the surface
$\vec{J}(\vec{r}')$	Current density in source region
$\vec{J}_s(\vec{r}')$	Current density restricted to the surface at point \vec{r}'
$\vec{H}_i(\vec{r}')$	Incident magnetic field at point \vec{r}'
$\vec{E}_i(\vec{r}')$	Incident electric field at point \vec{r}'
E_0	Magnitude of incident electric field in the vicinity of the surface
V'	Volume of source region
$\vec{E}_s(\vec{r})$	Scattered electric field at point \vec{r}
σ°	Normalized radar cross section
ω	Frequency of radar signal
k	Electromagnetic wave number of radar signal
f	Frequency of radar signal
μ_0	Permeability of space
η_0	Impedance of space
$\vec{G}(\vec{r}, \vec{r}')$	Dyadic Green's function
$g(\vec{r}, \vec{r}')$	Scalar Green's function
\vec{I}	Unit dyad
$\nabla\nabla$	3-dimensional dyadic operator

Table 2.2: Definition of symbols used in the backscatter derivation

antenna and that the electromagnetic fields are time harmonic. Based on these assumption, the follow approximations are valid:

$$\begin{aligned} |\vec{r} - \vec{r}'| &= r - \vec{r}' \cdot \hat{r} \\ \overline{\overline{G}}(\vec{r}, \vec{r}') &= (\overline{\overline{I}} - \hat{r}\hat{r}) \frac{e^{ikr}}{4\pi r} e^{-i\vec{k} \cdot \vec{r}'} \end{aligned} \quad (2.13)$$

where $\hat{r}\hat{r}$ represents an outer product.

Because the ocean surface is nearly a perfect conductor at microwave frequencies, the source current density is restricted to the surface. Hence,

$$\vec{J}(\vec{r}') = \vec{J}_s(\vec{r}') \delta[z' - \eta(x', y')]. \quad (2.14)$$

where $\eta(x', y')$ is the height of the surface at point (x', y') . The current on the surface can be found by boundary conditions:

$$\vec{J}_s(\vec{r}') = 2\hat{n} \times \vec{H}_i(\vec{r}') \big|_{z'=\eta(x', y')}. \quad (2.15)$$

where $\vec{H}_i(\vec{r}')$ is the incident magnetic field and \hat{n} is a unit vector normal to the surface. \hat{n} is given by

$$\hat{n} = \frac{\hat{z} - \frac{\partial \eta}{\partial x'} \hat{x} - \frac{\partial \eta}{\partial y'} \hat{y}}{\left[1 + \left(\frac{\partial \eta}{\partial x'}\right)^2 + \left(\frac{\partial \eta}{\partial y'}\right)^2\right]^{\frac{1}{2}}}. \quad (2.16)$$

Equation 2.15 models the surface current at each point as the current that would be present on the plane tangent to the surface at that point. This tangent plane approximation requires the radius of curvature of the surface to be large compared to an electromagnetic wavelength. This assumption holds for most surfaces of interest. As will be seen (Appendix B), the tangent plane approximation also does not account for any backscatter difference between horizontal and vertical polarizations.

Since it is assumed that the radar source is vertically polarized, the incident magnetic field is

$$\vec{H}_i(\vec{r}') = \hat{y} \frac{E_0}{\eta_0} e^{i\vec{k} \cdot \vec{r}'} = \hat{y} \frac{E_0}{\eta_0} e^{ik(x' \sin \theta_i - z' \cos \theta_i)}. \quad (2.17)$$

where E_0 is a constant and a function of the transmitted power.

Substituting Equations 2.16 and 2.17 into Equation 2.15 yields the following expression for the surface current,

$$\vec{J}_s(\vec{r}') = \left[-\hat{x} - \frac{\partial \eta}{\partial x'} \hat{z} \right] \frac{2E_0 e^{ik(x' \sin \theta_i - z' \cos \theta_i)}}{\eta_0 \left[1 + \left(\frac{\partial \eta}{\partial x'} \right)^2 + \left(\frac{\partial \eta}{\partial y'} \right)^2 \right]^{\frac{1}{2}}} \delta[z' - \eta(x'y')]. \quad (2.18)$$

This expression can then be substituted into Equation 2.10 to find an expression for the backscattered electric field.

$$\begin{aligned} \vec{E}_s(\vec{r}) &= \frac{-ikE_0}{2\pi r} e^{ikr} \int_{-\frac{1}{2}}^{\frac{1}{2}} dy' \int_{-\frac{1}{2}}^{\frac{1}{2}} dx' \int_{-\infty}^{\infty} dz' \delta[z' - \eta(x'y')] \cdot \\ &\quad \frac{\left[\hat{x}(\cos^2 \theta_i + \frac{1}{2} \frac{\partial \eta}{\partial x'} \sin 2\theta_i) + \hat{z}(\frac{\partial \eta}{\partial x'} \sin^2 \theta_i + \frac{1}{2} \sin 2\theta_i) \right]}{\left[1 + \left(\frac{\partial \eta}{\partial x'} \right)^2 + \left(\frac{\partial \eta}{\partial y'} \right)^2 \right]^{\frac{1}{2}}} e^{i2k(x' \sin \theta_i - z' \cos \theta_i)}. \end{aligned} \quad (2.19)$$

In Equation 2.19, the delta function integration can be performed resulting in

$$\begin{aligned} \vec{E}_s(\vec{r}) &= \frac{-ikE_0}{2\pi r} e^{ikr} \int_{-\frac{1}{2}}^{\frac{1}{2}} dy' \int_{-\frac{1}{2}}^{\frac{1}{2}} dx' \\ &\quad \left[\hat{x}(\cos^2 \theta_i + \frac{1}{2} \frac{\partial \eta}{\partial x'} \sin 2\theta_i) + \hat{z}(\frac{\partial \eta}{\partial x'} \sin^2 \theta_i + \frac{1}{2} \sin 2\theta_i) \right] \cdot \\ &\quad \frac{\left[1 + \left(\frac{\partial \eta}{\partial x'} \right)^2 + \left(\frac{\partial \eta}{\partial y'} \right)^2 + \left(\frac{\partial \eta}{\partial x'} \right)^2 \left(\frac{\partial \eta}{\partial y'} \right)^2 \right]^{\frac{1}{2}}}{\left[1 + \left(\frac{\partial \eta}{\partial x'} \right)^2 + \left(\frac{\partial \eta}{\partial y'} \right)^2 \right]^{\frac{1}{2}}} e^{i2k(x' \sin \theta_i - \eta(x',y') \cos \theta_i)}. \end{aligned} \quad (2.20)$$

On practical ocean surfaces, the slopes are much less than one. Hence, Equation 2.20 can be simplified by neglecting $\left(\frac{\partial \eta}{\partial x'} \right)^2 \left(\frac{\partial \eta}{\partial y'} \right)^2$. Further, $\frac{1}{2} \frac{\partial \eta}{\partial x'} \sin 2\theta_i$ and $\frac{\partial \eta}{\partial x'} \sin^2 \theta_i$ are negligible. Applying these approximations results in

$$\vec{E}_s(\vec{r}) = \frac{-ik \cos \theta_i E_0}{2\pi r} e^{ikr} (\hat{x} \cos \theta_i + \hat{z} \sin \theta_i) \int_{-\frac{1}{2}}^{\frac{1}{2}} dy' \int_{-\frac{1}{2}}^{\frac{1}{2}} dx' e^{i2k(x' \sin \theta_i - \eta(x',y') \cos \theta_i)}. \quad (2.21)$$

Because the backscattered power is proportional to $|\vec{E}_s(\vec{r})|^2$, Equation 2.21 is expanded to give an expression for $|\vec{E}_s(\vec{r})|^2$,

$$|\vec{E}_s(\vec{r})|^2 = \frac{k^2 \cos^2 \theta_i E_0^2}{4\pi^2 r^2} \int_{-\frac{1}{2}}^{\frac{1}{2}} dy' \int_{-\frac{1}{2}}^{\frac{1}{2}} dx' \int_{-\frac{1}{2}}^{\frac{1}{2}} dy \int_{-\frac{1}{2}}^{\frac{1}{2}} dx e^{i2k[(x'-x) \sin \theta_i + (\eta(x,y) - \eta(x',y')) \cos \theta_i]}. \quad (2.22)$$

This expression can be used to compute the normalized radar cross section, given by

$$\sigma^\circ = \frac{4\pi r^2}{L^2} \left\langle \frac{|\vec{E}_s(\vec{r})|^2}{E_0^2} \right\rangle. \quad (2.23)$$

The angle brackets in Equation 2.23 denote statistical expectation. Substituting Equation 2.22 into Equation 2.23 gives

$$\sigma^\circ = \frac{k^2 \cos^2 \theta_i}{\pi L^2} \int_{-\frac{L}{2}}^{\frac{L}{2}} dy' \int_{-\frac{L}{2}}^{\frac{L}{2}} dx' \int_{-\frac{L}{2}}^{\frac{L}{2}} dy \int_{-\frac{L}{2}}^{\frac{L}{2}} dx e^{i2k(x'-x) \sin \theta_i} \langle e^{i2k(\eta(x,y)-\eta(x',y')) \cos \theta_i} \rangle. \quad (2.24)$$

The quantity $\langle e^{i2k(\eta(x,y)-\eta(x',y')) \cos \theta_i} \rangle$ can be evaluated in terms of the characteristic function of the surface (Gray and Davisson, 1986, p. 257, Papoulis, 1991, p. 159); thus,

$$\langle e^{i2k(\eta(x,y)-\eta(x',y')) \cos \theta_i} \rangle = e^{-4\sigma^2 k^2 \cos^2 \theta_i (1-C_p(x-x',y-y'))}. \quad (2.25)$$

Substituting Equation 2.25 into Equation 2.24 and simplifying with the substitution $\alpha = x - x', \gamma = y - y'$ gives a form of the backscatter integral,

$$\sigma^\circ = \frac{k^2 \cos^2 \theta_i}{\pi} \int_{-L}^L d\alpha \int_{-L}^L d\gamma \left(1 - \frac{|\alpha|}{L}\right) \left(1 - \frac{|\gamma|}{L}\right) e^{-i2k\alpha \sin \theta_i} e^{-4\sigma^2 k^2 \cos^2 \theta_i (1-C_p(\alpha,\gamma))}. \quad (2.26)$$

This final form of the backscatter integral can be non-dimensionalized by substituting $u = \frac{\alpha}{L}$ and $v = \frac{\gamma}{L}$.

$$\sigma^\circ = \frac{(kL)^2 \cos^2 \theta_i}{\pi} \int_{-1}^1 du \int_{-1}^1 dv (1-|u|)(1-|v|) e^{-i2(kL)u \sin \theta_i} e^{-4(\sigma k)^2 \cos^2 \theta_i (1-C_p(uL,vL))}. \quad (2.27)$$

This integral is used to evaluate the backscatter, which is proportional to the normalized radar cross section.

2.3 Evaluation of the Backscatter Integral

Because of the complexity of the integrand, the backscatter integral (Equation 2.27) cannot be evaluated in closed form. In general, it must be evaluated numerically. Numerical evaluation is accomplished using a modified Romberg integration routine. In addition to numerical integration, when the power parameter of the surface (p) is not equal to 4 and the roughness of the surface (σk) is large,

the integral can be approximated asymptotically. Because the dominant term in the correlation coefficient is very complicated when $p = 4$, asymptotic evaluation as not attempted for this case. The asymptotic approximation is most useful when p is not close to 4. The closer p is to 4, the slower the asymptotic approximation converges to the true value. When these conditions for asymptotic approximation are not met, numerical integration must be employed to evaluate the backscatter integral.

2.3.1 Numerical evaluation

When numerically integrating a complicated function, such as the backscatter integral (Equation 2.27), care must be taken to ensure correct results. If the integration step size is too large, for example, the numerical result may not converge, or it may converge to an incorrect value. Numerically integrating the backscatter integral is particularly difficult because the integrand contains an oscillatory term. Due to this oscillatory term, extra care must be taken to avoid evaluating the function only at maxima (or minima) of the oscillation. Because of the oscillatory term in the integrand, a generalized Romberg numerical integration routine is used to evaluate the backscatter integral. The generalized Romberg routine avoids evaluating the function only at maxima or minima by varying the step size between points where the integrand is evaluated. In addition, since the period of oscillation in the backscatter integrand is known, (the period is given by $2(kL) \sin \theta_i$), it is insured that step size is sufficiently small to avoid problems. In addition to varying the step size, the generalized Romberg routine also uses extrapolation to find the value of the integral with maximum computational efficiency.

To further insure that the numerical integration is producing correct values, it is useful to check some limiting cases. Figures 2.7 and 2.8 in Section 2.3.2 show that when the surface roughness is large, the asymptotic approximations converge to the corresponding numerically integrated curves. In addition, when the surface roughness is very small, the $e^{-4(\sigma k)^2 \cos^2 \theta_i (1 - C_p(uL, vL))}$ term in the backscatter integral can be approximated by the first term of its Taylor series. With this

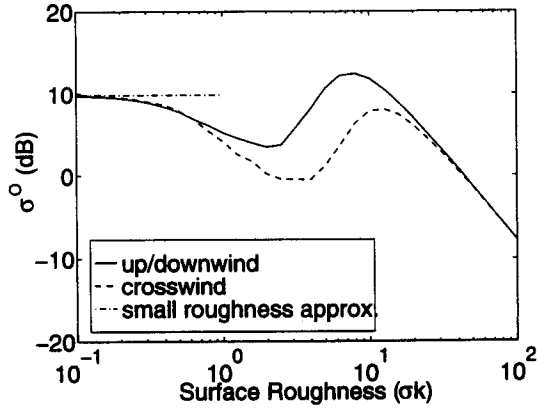


Figure 2.6: Results of integrating the backscatter integral with a modified Romberg routine. The plots were generated with $p = 4.0$, $k_0 = 1.5m^{-1}$, $\theta_0 = 90^\circ$, $\theta_i = 10^\circ$, and $f = 10GHz$ ($k = 209m^{-1}$). Up/downwind corresponds to $\theta_{Az} = 0^\circ$, and crosswind corresponds to $\theta_{Az} = 90^\circ$

approximation, the integral can be evaluated in closed form, giving

$$\sigma^o \approx \frac{1 - \cos[2(kL) \sin \theta_i]}{2\pi \tan^2 \theta_i} \quad (2.28)$$

as a small roughness approximation. The small roughness approximation has been included in Figure 2.6, which gives some examples of the results of numerically integrating the backscatter integral. The figure shows that the numerical results converge to the small roughness approximation when the surface roughness is small. Confidence is gained in the numerical results by knowing that they converge to the appropriate approximations for extreme values of surface roughness.

2.3.2 Asymptotic evaluation

As noted previously, the backscatter integral can be approximated asymptotically when the roughness (σk) is large. If the roughness of the surface is large, the integrand in Equation 2.27 is very small unless $C_p(uL, vL)$ is very close to one. $C_p(uL, vL)$ is very close to one when u and v are close to zero, or in polar coordinates, when ρ is close to zero. Since the integrand is small unless ρ is near zero, the correlation coefficient can be approximated by its dominant term. The first three terms of the correlation coefficient are $C_p(\rho L, \phi) = 1 - T_1(\phi)(\rho L)^{p-2} - T_2(\phi)(\rho L)^2$

where

$$T_1(\phi) = \frac{(2-p)}{\frac{\pi}{3}\theta_0\text{erf}\left(\frac{\sqrt{3}\pi}{2\theta_0}\right)} \cos\left[\frac{\pi}{2}(p-2)\right] \Gamma(2-p) k_0^{p-2} \cdot \int_{\theta_{Az}-\frac{\pi}{2}}^{\theta_{Az}+\frac{\pi}{2}} d\theta |\cos(\theta-\phi)|^{p-2} \exp\left[-3\left(\frac{\theta-\theta_{Az}}{\theta_0}\right)^2\right] \quad (2.29)$$

and

$$T_2(\phi) = \frac{(2-p)k_0^2}{2(4-p)\frac{\pi}{3}\theta_0\text{erf}\left(\frac{\sqrt{3}\pi}{2\theta_0}\right)} \int_{\theta_{Az}-\frac{\pi}{2}}^{\theta_{Az}+\frac{\pi}{2}} d\theta \cos^2(\theta-\phi) \exp\left[-3\left(\frac{\theta-\theta_{Az}}{\theta_0}\right)^2\right]. \quad (2.30)$$

When $p < 4$ the $(\rho L)^{p-2}$ term dominates, whereas for $p > 4$, the $(\rho L)^2$ term dominates. Thus, for asymptotic evaluation, when $p < 4$, the correlation coefficient is taken to be $C_p(\rho, \phi) \approx 1 - T_1(\phi)(\rho L)^{p-2}$, and when $p > 4$, the correlation coefficient is approximated by $C_p(\rho, \phi) \approx 1 - T_2(\phi)(\rho L)^2$.

Because the integrand is very small except when u and v are near zero, the integral can be simplified by neglecting the $(1 - |u|)$ and $(1 - |v|)$ terms. Also, the limits of integration can be extended, resulting in

$$\sigma^\circ = \frac{(kL)^2 \cos^2 \theta_i}{\pi} \int_{-\infty}^{\infty} du \int_{-\infty}^{\infty} dv e^{-i2(kL)u \sin \theta_i} e^{-4(\sigma k)^2 \cos^2 \theta_i (1 - C_p(uL, vL))}. \quad (2.31)$$

While Equation 2.31 is useful for some asymptotic evaluations, It is also useful to consider polar coordinates. After conversion to polar coordinates, Equation 2.31 is given by

$$\sigma^\circ = \frac{(kL)^2 \cos^2 \theta_i}{\pi} \int_0^{2\pi} d\phi \int_0^{\infty} d\rho \rho e^{-i2(kL) \sin \theta_i \rho \cos \phi} e^{-4(\sigma k)^2 \cos^2 \theta_i (1 - C_p(\rho L, \phi))}. \quad (2.32)$$

Asymptotic evaluation for $p < 4$

Because the dominant term that dominates changes when $p = 4$, it is necessary to consider the cases $p < 4$ and $p > 4$ separately. The case $p < 4$ is considered first. Substituting the dominant term for the correlation coefficient into Equation 2.32 gives

$$\sigma^\circ = \frac{(kL)^2 \cos^2 \theta_i}{\pi} \int_0^{2\pi} d\phi \int_0^{\infty} d\rho \rho e^{-i2(kL) \sin \theta_i \rho \cos \phi} e^{-4(\sigma k)^2 \cos^2 \theta_i T_1(\phi)(\rho L)^{p-2}}. \quad (2.33)$$

For convenience in the derivation, the following are defined:

$$\begin{aligned} A &= \frac{(kL)^2 \cos^2 \theta_i}{\pi} \\ B &= 2(kL) \sin \theta_i \\ C &= 4(\sigma k)^2 \cos^2 \theta_i. \end{aligned} \quad (2.34)$$

With these definitions, Equation 2.33 becomes

$$\sigma^\circ = A \int_0^{2\pi} d\phi \int_0^\infty d\rho \rho e^{-iB\rho \cos \phi} e^{-CT_1(\phi)(\rho L)^{p-2}}. \quad (2.35)$$

Because the $e^{-CT_1(\phi)\rho^{p-2}}$ term in Equation 2.35 approaches zero rapidly as ρ gets larger, the $e^{-iB\rho \cos \phi}$ can be approximated by the first three terms of its Taylor Series. This gives

$$\sigma^\circ = A \int_0^{2\pi} d\phi \int_0^\infty d\rho \rho (1 - iB\rho \cos \phi - B^2 \rho^2 \cos^2 \phi) e^{-CT_1(\phi)(\rho L)^{p-2}}. \quad (2.36)$$

Substituting $t = CT_1(\phi)(\rho L)^{p-2}$ gives

$$\begin{aligned} \sigma^\circ &= A \int_0^{2\pi} d\phi \left[\frac{(CT_1(\phi))^{-2/(p-2)}}{L^2(p-2)} \int_0^\infty dt t^{(4-p)/(p-2)} e^{-t} \right. \\ &+ \frac{-iB \cos \phi (CT_1(\phi))^{-3/(p-2)}}{L^3(p-2)} \int_0^\infty dt t^{(5-p)/(p-2)} e^{-t} \\ &\left. - \frac{B^2 \cos^2 \phi (CT_1(\phi))^{-4/(p-2)}}{L^4(p-2)} \int_0^\infty dt t^{(6-p)/(p-2)} e^{-t} \right]. \end{aligned} \quad (2.37)$$

The integrals in Equation 2.37 can be evaluated in terms of the gamma function, giving

$$\begin{aligned} \sigma^\circ &= A \int_0^{2\pi} d\phi \left[\frac{(CT_1(\phi))^{-2/(p-2)}}{L^2(p-2)} \Gamma\left(\frac{2}{p-2}\right) \right. \\ &+ \frac{-iB \cos \phi (CT_1(\phi))^{-3/(p-2)}}{L^3(p-2)} \Gamma\left(\frac{3}{p-2}\right) \\ &\left. - \frac{B^2 \cos^2 \phi (CT_1(\phi))^{-4/(p-2)}}{L^4(p-2)} \Gamma\left(\frac{4}{p-2}\right) \right]. \end{aligned} \quad (2.38)$$

In Equation 2.38, $T_1(\phi)$ is periodic with period π . In the second term of the Equation 2.38, $T_1(\phi)$ is multiplied by $\cos \phi$ which has the property $\cos(\phi + \pi) = -\cos \phi$. Thus, when this term is integrated with respect to ϕ , the result is zero.

Substituting the definitions for A , B , C , and $T_1(\phi)$ into the remaining terms and rearranging gives an approximation for σ° when $p < 4$:

$$\begin{aligned} \sigma^\circ \approx & \frac{X}{\pi(p-2)} \left[\Gamma\left(\frac{2}{p-2}\right) \int_0^{2\pi} d\phi I_3(\phi)^{-2/(p-2)} \right. \\ & \left. - 4X \tan^2 \theta_i \Gamma\left(\frac{4}{p-2}\right) \int_0^{2\pi} d\phi \cos^2 \phi I_3(\phi)^{-4/(p-2)} \right] \end{aligned} \quad (2.39)$$

where

$$I_3(\phi) = \int_{\theta_{Az}-\frac{\pi}{2}}^{\theta_{Az}+\frac{\pi}{2}} d\theta |\cos(\theta - \phi)|^{p-2} \exp \left[-3 \left(\frac{\theta - \theta_{Az}}{\theta_0} \right)^2 \right] \quad (2.40)$$

and

$$X = \frac{(\sigma k \cos \theta_i)^{2(p-4)/(p-2)} \left(\frac{\pi}{3} \theta_0 \operatorname{erf} \left(\frac{\sqrt{3}\pi}{2\theta_0} \right) \right)^{2/(p-2)}}{\left[4(2-p)\Gamma(2-p) \cos \left(\frac{\pi}{2}(p-2) \right) \right]^{2/(p-2)} (\sigma k_0)^2} \quad (2.41)$$

Unfortunately, Equation 2.39 is clumsy because it still contains two-dimensional integrals which must be numerically evaluated. These integrals have carried over from the derivation of the correlation coefficient of the surface. While they do make Equation 2.39 clumsy, the integrands are not oscillatory over the area of integration as is the case with the backscatter integral. Further, the integrands in Equation 2.37 are simple enough to be readily approximated by trapezoidal integration. These properties make Equation 2.39 much easier to numerically evaluate than is the backscatter integral. Plots comparing the results of Equation 2.39 to numerical evaluations of the backscatter integral are in Figure 2.7. The plots show that the asymptotic approximation converges to the numerical result as the roughness gets larger. In the specific case shown ($p = 3.5$, $k_0 = 1.5m^{-1}$, $\theta_0 = 90^\circ$, $\theta_i = 10^\circ$, and $f = 10\text{GHz}$ ($k = 209m^{-1}$)), the asymptotic approximation is valid for a roughness greater than approximately 2.

Asymptotic evaluation for $p > 4$

As previously mentioned, when evaluating the backscatter integral asymptotically, it is necessary to consider the case $p > 4$ separately from the case $p < 4$. When $p > 4$, the correlation coefficient is dominated by

$$C_p(\rho L, \phi) \approx 1 - T_2(\phi)(\rho L)^2 \quad (2.42)$$

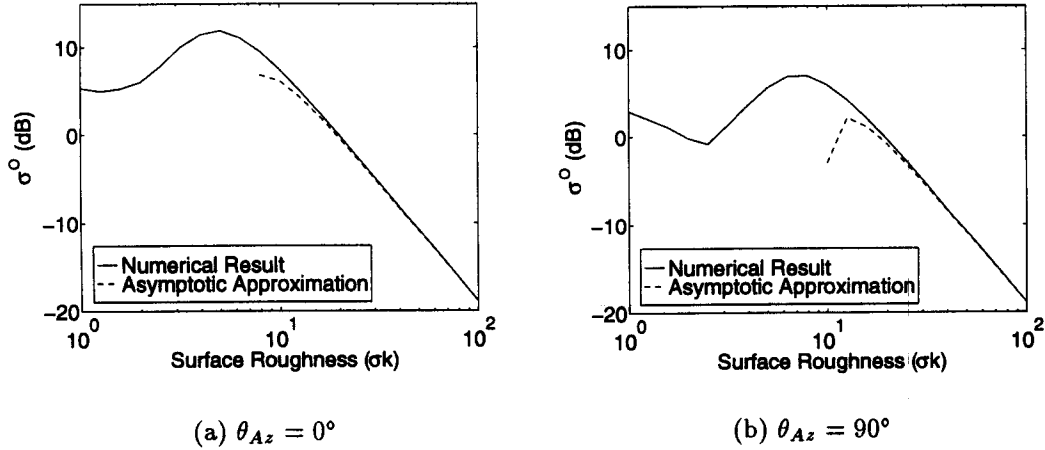


Figure 2.7: Comparison of the asymptotic expansions for $p < 4$ with the numerical results. For the plots, $p = 3.5$, $k_0 = 1.5m^{-1}$, $\theta_0 = 90^\circ$, $\theta_i = 10^\circ$, and $f = 10GHz$ ($k = 209m^{-1}$).

where $T_2(\phi)$ is given by Equation 2.30. Substituting into Equation 2.32 yields

$$\sigma^0 = \frac{(kL)^2 \cos^2 \theta_i}{\pi} \int_0^{2\pi} d\phi \int_0^\infty d\rho \rho e^{-i2(kL) \sin \theta_i \rho \cos \phi} e^{-4(\sigma k)^2 \cos^2 \theta_i T_2(\phi) (\rho L)^2}. \quad (2.43)$$

At this point, steps that exactly parallel the asymptotic derivation for $p < 4$ can be performed, resulting in

$$\sigma^0 \approx \frac{X}{2\pi} \left(\int_0^{2\pi} d\phi I_4(\phi)^{-1} - 4X \tan^2 \theta_i \int_0^{2\pi} d\phi \cos^2 \phi I_4(\phi)^{-2} \right) \quad (2.44)$$

where

$$I_4(\phi) = \int_{\theta_{Az} - \frac{\pi}{2}}^{\theta_{Az} + \frac{\pi}{2}} d\theta \cos^2(\theta - \phi) \exp \left[-3 \left(\frac{\theta - \theta_{Az}}{\theta_0} \right)^2 \right] \quad (2.45)$$

and

$$X = \left(\frac{p-4}{p-2} \right) \frac{\frac{\pi}{3} \theta_0 \operatorname{erf} \left(\frac{\sqrt{3}}{2\theta_0} \right)}{2(\sigma k_0)^2} \quad (2.46)$$

As in the case for $p < 4$, Equation 2.44 contains two-dimensional integrals that must be numerically evaluated. These integrals are much easier to evaluate than is the entire backscatter integral. However, unlike the $p < 4$ case, it is possible to find an asymptotic expansion that does not contain numerical integrals. Doing so requires an approximation to be made to $W(\theta)$, the function describing the directionality of the waves on the ocean surface. Recall from

Equation 2.3 that

$$W(\theta) = \exp \left[-3 \left(\frac{\theta - \theta_{Az}}{\theta_0} \right)^2 \right], \quad \theta_{Az} - \frac{\pi}{2} \leq \theta \leq \theta_{Az} + \frac{\pi}{2}. \quad (2.47)$$

For purposes of the asymptotic evaluation, this function is approximated with a rect function, given by

$$W'(\theta) = \begin{cases} 1 & \theta_{Az} - \frac{\theta_0}{2} \leq \theta \leq \theta_{Az} + \frac{\theta_0}{2} \\ 0 & \text{otherwise} \end{cases} \quad (2.48)$$

Replacing $W(\theta)$ with $W'(\theta)$ slightly overestimates the backscatter, it will be shown that the error is not severe (Figure 2.8). Replacing $W(\theta)$ with $W'(\theta)$ also requires that S_0 , the normalization factor for the correlation coefficient, be modified. The area under $W(\theta)$ must be replaced with the area under $W'(\theta)$. Thus, $\frac{\pi}{3}\theta_0\text{erf}\left(\frac{\sqrt{3}\pi}{2\theta_0}\right)$ is replaced with θ_0 . With these modifications, the dominant behavior of the correlation coefficient becomes

$$C_p(\rho L, \phi) \approx 1 - T'_2(\phi)(\rho L)^2 \quad (2.49)$$

where

$$T'_2(\phi) = \frac{(p-2)k_0^2}{2(p-4)\theta_0} \int_{\theta_{Az}-\frac{\theta_0}{2}}^{\theta_{Az}+\frac{\theta_0}{2}} d\theta \cos^2(\theta - \phi). \quad (2.50)$$

The integral in $T'_2(\phi)$ can now be evaluated in closed form, giving

$$T'_2(\phi) = \left(\frac{p-2}{p-4} \right) \left(\frac{k_0^2}{8\theta_0} \right) (2\theta_0 - \sin[2\phi - (2\theta_{Az} + \theta_0)] + \sin[2\phi - (2\theta_{Az} - \theta_0)]). \quad (2.51)$$

$T'_2(\phi)$ can be converted to rectangular coordinates and substituted into Equation 2.31. The integral in Equation 2.31 can then be evaluated using the saddle point method. To simplify equations, define

$$K = \left(\frac{p-2}{p-4} \right) \left(\frac{k_0^2}{8\theta_0} \right). \quad (2.52)$$

Equation 2.51 can be rewritten, using trigonometric identities, as

$$\begin{aligned} T'_2(\phi) &= K \{ 2\theta_0 + \sin 2\phi [\cos(2\theta_{Az} - \theta_0) - \cos(2\theta_{Az} + \theta_0)] \\ &\quad + \cos 2\phi [\sin(2\theta_{Az} + \theta_0) - \sin(2\theta_{Az} - \theta_0)] \} \end{aligned} \quad (2.53)$$

Noting that $\sin 2\phi = \frac{2 \tan \phi}{1 + \tan^2 \phi}$, $\cos 2\phi = \frac{1 - \tan^2 \phi}{1 + \tan^2 \phi}$, and $\tan \phi = \frac{vL}{uL}$, Equation 2.53 can be rewritten as

$$\begin{aligned}
T_2'(uL, vL) &= K \left\{ 2\theta_0 + \frac{(vL)/(uL)}{1 + (vL)^2/(uL)^2} [\cos(2\theta_{Az} - \theta_0) - \cos(2\theta_{Az} + \theta_0)] \right. \\
&\quad \left. + \frac{1 - (vL)^2/(uL)^2}{1 + (vL)^2/(uL)^2} [\sin(2\theta_{Az} + \theta_0) - \sin(2\theta_{Az} - \theta_0)] \right\} \\
&= \frac{K}{(uL)^2 + (vL)^2} \{ 2\theta_0 [(uL)^2 + (vL)^2] \\
&\quad + 2(uL)(vL) [\cos(2\theta_{Az} - \theta_0) - \cos(2\theta_{Az} + \theta_0)] \\
&\quad + [(uL)^2 - (vL)^2] [\sin(2\theta_{Az} + \theta_0) - \sin(2\theta_{Az} - \theta_0)] \} \\
&= \frac{K}{(uL)^2 + (vL)^2} \{ (uL)^2 [2\theta_0 + \sin(2\theta_{Az} + \theta_0) - \sin(2\theta_{Az} - \theta_0)] \\
&\quad + (uL)(vL) [2 \cos(2\theta_{Az} - \theta_0) - 2 \cos(2\theta_{Az} + \theta_0)] \\
&\quad + (vL)^2 [2\theta_0 - \sin(2\theta_{Az} + \theta_0) + \sin(2\theta_{Az} - \theta_0)] \} \\
&= \frac{1}{(uL)^2 + (vL)^2} (A(uL)^2 + B(uL)(vL) + C(vL)^2) \tag{2.54}
\end{aligned}$$

where

$$\begin{aligned}
A &= K [2\theta_0 + \sin(2\theta_{Az} + \theta_0) - \sin(2\theta_{Az} - \theta_0)] \\
B &= K [2 \cos(2\theta_{Az} - \theta_0) - 2 \cos(2\theta_{Az} + \theta_0)] \\
C &= K [2\theta_0 - \sin(2\theta_{Az} + \theta_0) + \sin(2\theta_{Az} - \theta_0)]. \tag{2.55}
\end{aligned}$$

Since $(\rho L)^2 = (uL)^2 + (vL)^2$, it follows that $T_2'(\phi)(\rho L)^2 = A(uL)^2 + B(uL)(vL) + C(vL)^2$.

Using Equation 2.49 in Equation 2.31 gives an integral that can be evaluated asymptotically by the saddle point method,

$$\sigma^\circ = \frac{(kL)^2 \cos^2 \theta_i}{\pi} \int_{-\infty}^{\infty} du \int_{-\infty}^{\infty} dv e^{-i2(kL)u \sin \theta_i} e^{-4(\sigma k)^2 \cos^2 \theta_i (A(uL)^2 + B(uL)(vL) + C(vL)^2)}. \tag{2.56}$$

Proceeding with the saddle point method as outlined by (Kong, 1990, pp. 307-309), the saddle point with respect to v is $v_0 = \frac{-Bu}{2C}$. Keeping one term of the asymptotic series,

$$\sigma^\circ \approx \frac{kL \cos \theta_i}{2\sigma \sqrt{\pi C}} \int_{-\infty}^{\infty} du e^{-i2(kL)u \sin \theta_i} e^{-4(\sigma k)^2 \cos^2 \theta_i (uL)^2 (A - \frac{B^2}{4C})}. \tag{2.57}$$

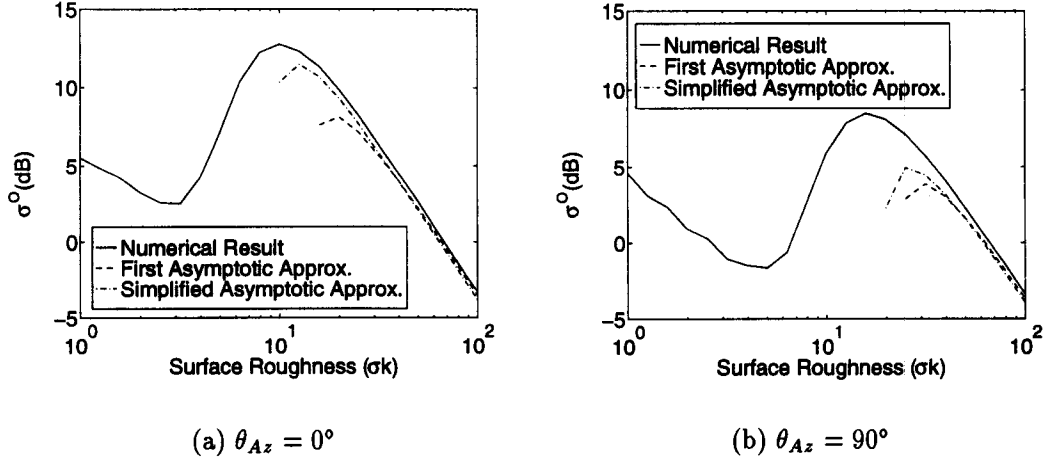


Figure 2.8: Comparison of the asymptotic expansions for $p > 4$ with the numerical results. For the plots, $p = 4.5$, $k_0 = 1.5m^{-1}$, $\theta_0 = 90^\circ$, $\theta_i = 10^\circ$, and $f = 10\text{GHz}$ ($k = 209m^{-1}$). The first asymptotic expansion is calculated from Equation 2.44, and the simplified asymptotic expansion from Equation 2.59

Applying the saddle point method a second time, the saddle point is found to be $u_0 = 0$. Keeping two terms of the asymptotic series (two terms are kept to preserve the behavior of the $e^{-i2(kL)u \sin \theta_i}$ term) yields

$$\sigma^o \approx \frac{1}{2\sigma^2 \sqrt{4AC - B^2}} \left(1 - \frac{C \tan^2 \theta_i}{\sigma^2(4AC - B)} \right). \quad (2.58)$$

Substituting the definitions of A , B , and C ,

$$\sigma^o \approx \frac{X}{\sqrt{\theta_0^2 - \sin^2 \theta_0}} \left(1 - \left[\frac{X \tan^2 \theta_i}{2} \right] \frac{2\theta_0 - \sin(2\theta_{Az} + \theta_0) + \sin(2\theta_{Az} - \theta_0)}{\theta_0^2 - \sin^2 \theta_0} \right) \quad (2.59)$$

where

$$X = \left(\frac{p-4}{p-2} \right) \frac{\theta_0}{(\sigma k_0)^2}. \quad (2.60)$$

Plots showing the numerical results of the backscatter integral and the results of Equations 2.44 and 2.59 are shown in Figure 2.8. As is the case with $p < 4$, the asymptotic approximation converges to the numerical result as the roughness gets larger. For the specific case shown ($p = 4.5$, $k_0 = 1.5m^{-1}$, $\theta_0 = 90^\circ$, $\theta_i = 10^\circ$, and $f = 10\text{GHz}$ ($k = 209m^{-1}$)), the asymptotic result is valid when the roughness is larger than approximately 4. The plots also show that the error

due to the approximation used in deriving the simplified asymptotic approximation (Equation 2.59) is much less than 1 dB when the surface roughness is larger than 4. When the roughness is less than 4, the surface is too smooth to permit asymptotic evaluation.

2.4 Summary

The theory to predict the backscatter from a randomly rough ocean surface has been derived. First, the ocean was modeled as a stochastic process. The statistics were assumed to be Gaussian, and the mean, variance, and correlation coefficient were characterized. Using the surface model, the tangent plane approximation, and Green's theorem, the expected backscatter was derived. The result was Equation 2.27, the backscatter integral. When $p \neq 4$ and the roughness of the surface is high, the backscatter integral can be approximated asymptotically. Otherwise, it must be evaluated numerically.

The backscatter integral can now be used to predict the the backscatter expected from a random surface. In general, the predicted backscatter will be a function of the azimuth angle (θ_{Az}). Thus, the theory will be used to predict azimuth modulation of the radar backscatter.

THEORETICAL AZIMUTH MODULATION AT NEAR-NORMAL INCIDENCE

The theory derived in Chapter 2 predicts azimuth modulation of the radar backscatter at near-normal incidence angles. When the normalized radar cross section is plotted as a function of azimuth angle (holding the other parameters fixed), the difference (in decibels) between its maximum value and its minimum value is defined as the azimuth modulation magnitude. Directed surfaces, that is, surfaces for which the power spectral density is a function of wave direction lead to azimuth modulation. However, when a directed surface becomes very rough, it scatters power in nearly every direction, and the modulation disappears. In general, the modulation magnitude also depends on the surface parameters (p , k_0 , and θ_0) as well as the radar incidence angle (θ_i) and frequency (f).

3.1 Physical Discussion

It has been shown (Figure 2.6, repeated in Figure 3.1 for convenience) that there is little azimuth modulation from a the surface that is very smooth. In fact, when the surface is very smooth, there is little backscattered power unless $\theta_i = 0$. Figure 3.1 shows that when all other parameters are fixed, the magnitude of the modulation peaks for some moderate value of surface roughness. As the surface becomes progressively more rough, the modulation decreases, eventually disappearing for very rough surfaces. To gain some intuition about these trends, consider some simplified scattering problems.

3.1.1 Scattering from a flat surface versus a rough surface

First, consider a scattering surface that is perfectly flat, or in other words, a surface with standard deviation of $\sigma = 0$. If $\theta_i = 0$, the path of the incident electromagnetic wave is vertical toward the surface. At the surface, the wave is reflected, and the reflected (scattered) wave returns to the antenna along

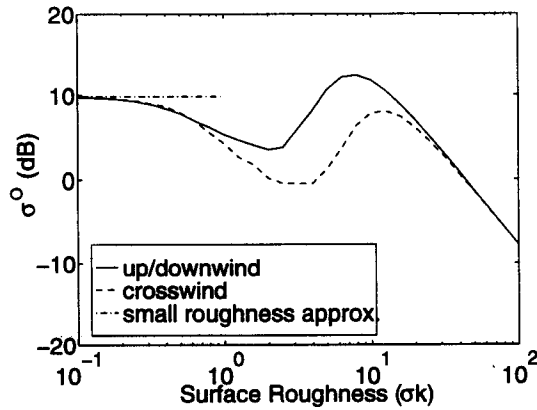


Figure 3.1: Results of integrating the backscatter integral with a modified Romberg routine. The plots were generated with $p = 4.0$, $k_0 = 1.5m^{-1}$, $\theta_0 = 90^\circ$, $\theta_i = 10^\circ$, and $f = 10\text{GHz}$ ($k = 209m^{-1}$). Up/downwind corresponds to $\theta_{Az} = 0^\circ$, and crosswind corresponds to $\theta_{Az} = 90^\circ$

the same path traversed by the incident wave. However, if $\theta_i > 0$, the incident wave is reflected according to Snell's law, as shown in Figure 3.2. Little, if any, scattered power will return to the antenna, regardless of the azimuth angle. Thus, there is no azimuth modulation.

Now consider the case where the surface begins to become rough. For rough surfaces, $\sigma > 0$, and the larger the value of σ , the rougher the surface. If $\theta_i > 0$, there may be some facets of the surface perpendicular to the path of the incident electromagnetic wave. These facets scatter power back toward the antenna. The amount of power that is backscattered depends on the number and size of the facets that are perpendicular to the incident path. The number and size of the perpendicular facets in turn depends on the roughness of the surface and the incidence angle (θ_i). If θ_i is larger, the surface must become more rough before the perpendicular facets become significant. Further, the surface may be directed, or have a preferred direction of wave travel. If the surface is directed, the number and size of the facets perpendicular to the incident electromagnetic path depends on the radar azimuth angle (θ_{Az}).

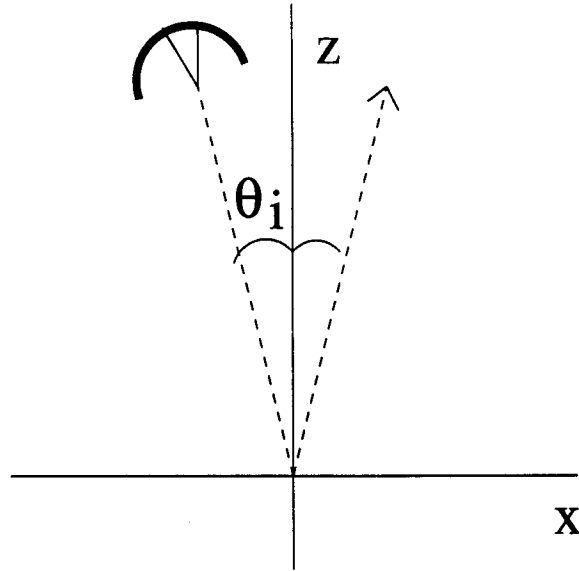


Figure 3.2: Scattering from a perfectly flat surface ($\sigma = 0$).

3.1.2 Scattering from a unidirectional surface

To better understand the dependence of the perpendicular facets on azimuth angle, consider a unidirectional surface, or a surface with waves traveling in only one direction. For simplicity, assume further that a single wavenumber is present on the surface. Such a surface is depicted in Figure 3.3; with the perpendicular facets highlighted. The figure shows that there are more perpendicular facets when $\theta_{Az} = 0^\circ$ (Figure 3.3a) than when $\theta_{Az} = 90^\circ$ (Figure 3.3b). This leads to more backscattered power when $\theta_{Az} = 0^\circ$ than when $\theta_{Az} = 90^\circ$. For surfaces less directed than Figure 3.3, the dependence of the backscatter on the azimuth angle is less pronounced, but some dependence is still present.

3.1.3 Scattering from a random, rough surface

For very smooth surfaces, the azimuth modulation increases as a function of surface roughness (see Figure 3.1). However, as Figure 3.1 also shows, when the surface becomes progressively more rough, the azimuth modulation begins to decrease. In fact, when the surface is very rough, the azimuth modulation disappears altogether. To understand this modulation decrease, consider Figure 3.4. Figures 3.4a and b depict a moderately rough surface ($\sigma = 0.04m$) while the

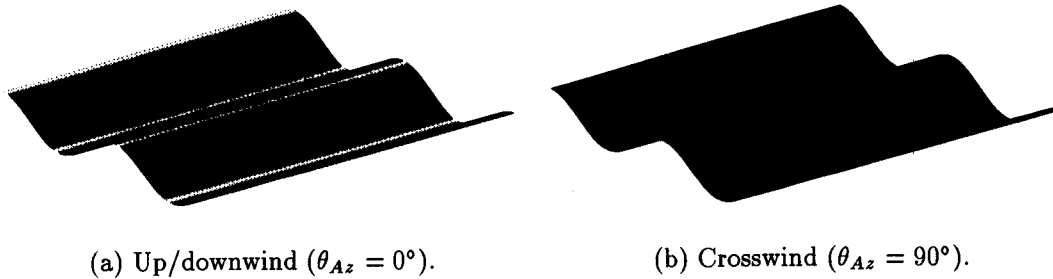


Figure 3.3: Scattering from a unidirectional surface. Facets perpendicular to the incident electromagnetic path ($\theta_i = 10^\circ$) are highlighted. The backscatter in the up/downwind case is greater than in the crosswind case.

surface in Figures 3.4c and d is 2.5 times as rough ($\sigma = 0.1m$). The surfaces were generated using a Gaussian random number generator and filtering the output to create the correct power spectral density. The highlighted portions of each surface are the facets that are perpendicular to the incident electromagnetic path. Notice the contrast in facets between the $\theta_{Az} = 0^\circ$ and the $\theta_{Az} = 90^\circ$ cases. When the surface is rougher, there is less difference in the size of the perpendicular facets. This translates into less azimuth modulation. Practical ocean surfaces almost always exhibit the characteristic of decreasing modulation with increasing roughness; the surface is seldom smooth enough to observe increasing modulation with increasing roughness.

3.2 Sensitivity of Azimuth Modulation to Model Parameters

To further understand the azimuth modulation, it is instructive to study its sensitivity to the various model parameters. Specifically, the parameters of interest are the surface parameters, which are the power parameter (p), the spectral peak (k_0), and the directional parameter (θ_0); and the radar parameters, which are the incidence angle (θ_i) and the frequency (f). Each of these parameters is discussed in turn. The modulation trends are discussed in terms of practical surfaces, that is, surfaces that are sufficiently rough that the modulation is decreasing with increasing roughness.

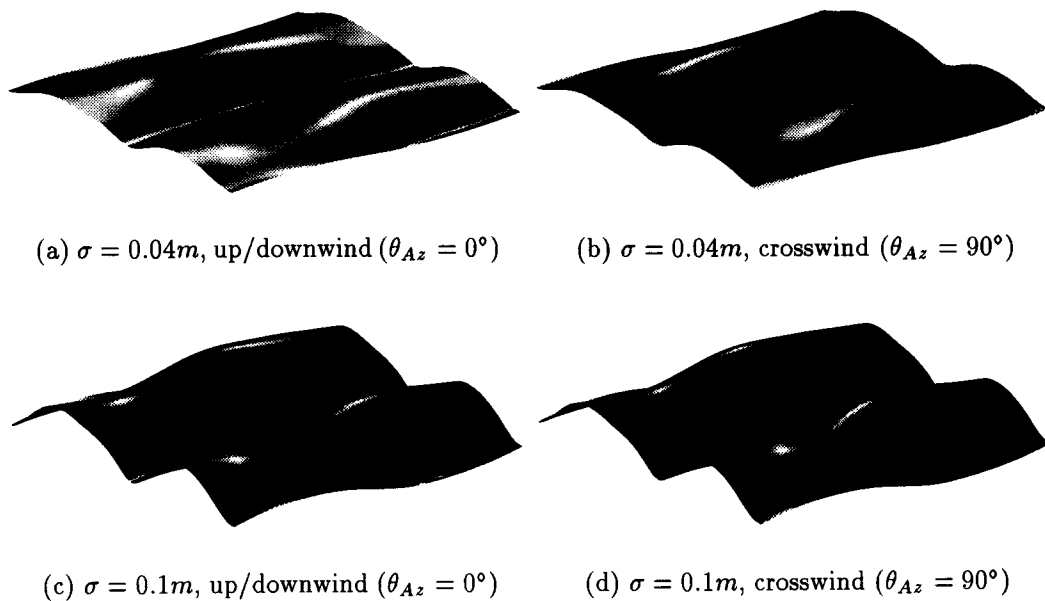


Figure 3.4: Scattering from rough surfaces. The highlighted portions of the surface are the facets that are perpendicular to the incident electromagnetic path. Note the difference in the facets between the up/downwind case and the crosswind case for each surface. The rougher surface scatters power in more directions and exhibits less azimuth modulation. The surfaces depicted are $1.28m \times 1.28m$ in size, and the parameters are $p = 4.0$, $k_0 = 1.5m^{-1}$, $\theta_0 = 90^\circ$, and $\theta_i = 10^\circ$.

3.2.1 Dependence on the power parameter (p)

The dependence of the azimuth modulation on the power parameter is as shown in Figure 3.5. As seen in the figure, a surfaces with a roughness of approximately 10 have modulations that vary as a function of p . When $p = 3.5$, the modulation is about 1.5dB; when p increases to 4.0, the modulation increases to about 4dB, and finally, when p has increased to 4.5, the modulation has again increased to approximately 6.75dB. Thus, the modulation is increasing with increasing p values. To understand this trend, consider the effect of p on the power spectral density of the surface. The model for power spectral density is k_w^{-p} . If p is smaller, the spectral power falls off less rapidly with increasing wave number. Since larger wave numbers correspond to larger slopes on the surface, smaller p values allow larger slopes to be present on the surface. Hence, the slope variance on the surface is larger. A larger slope variance leads to surface facets pointing in more directions, which allows the surface to scatter power in more directions. When the surface is scattering power in more directions, the azimuth modulation is decreased.

3.2.2 Dependence on the low wave number cut-off (k_0)

It should be clear from the plots in Figure 3.6 that the azimuth modulation decreases with increasing values of the spectral peak, k_0 . For a roughness of 10, a k_0 of $0.5m^{-1}$ corresponds to a modulation of approximately 9dB, while k_0 values of $1.5m^{-1}$ and 4.5^{-1} correspond to modulations of 4dB and 0.5dB respectively. To understand this trend, consider the relationship between the surface variance σ^2 , and the power spectral density. The surface variance is the integral of the power spectral density. Thus, for a fixed σ and a power spectral density of the form $k_w^{-p}u(k_w - k_0)$, a larger k_0 corresponds to a surface with more power at larger wavenumbers. Larger wave numbers lead to larger slopes and more slope variance on the surface. This leads to surface facets pointing in more directions. Facets pointing in more directions lead to power being scattered in more directions, which decreases the azimuth modulation. Thus, the modulation decreases with increasing k_0 .

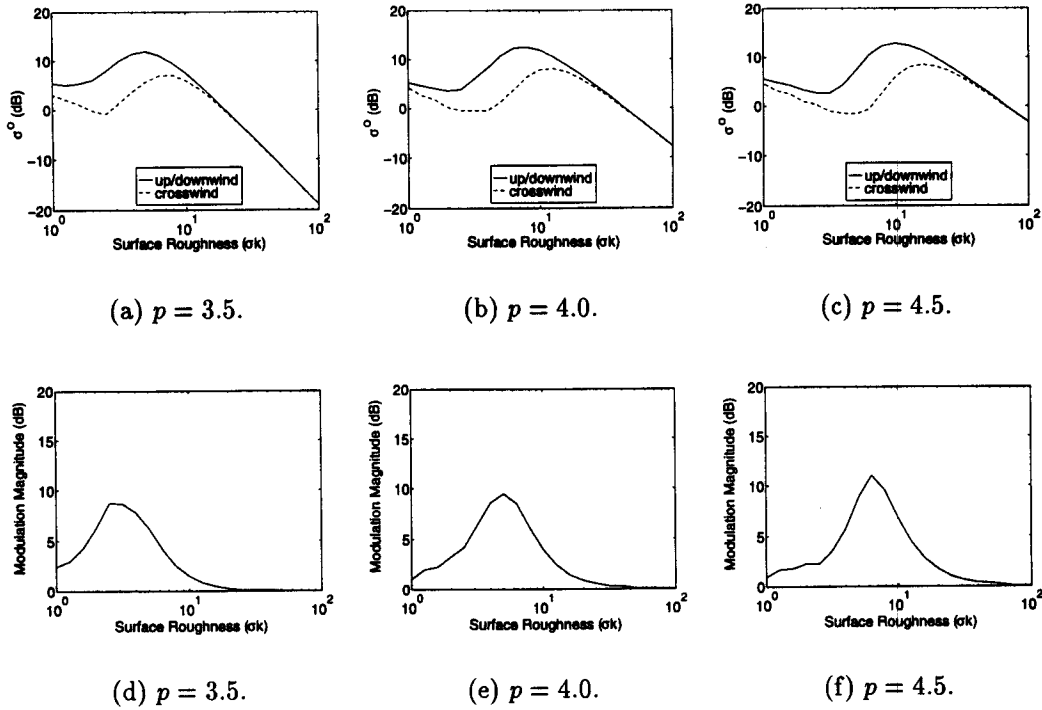


Figure 3.5: Dependence of the modulation on the power parameter (p). The plots were generated using $k_0 = 1.5m^{-1}$, $\theta_0 = 90^\circ$, $\theta_i = 10^\circ$, and $f = 10GHz$ ($k = 209m^{-1}$). The top row of figures shows σ^0 for $\theta_{Az} = 0^\circ$ (up/downwind) and $\theta_{Az} = 90^\circ$ (crosswind). The bottom row shows the modulation magnitude, which is the difference between the $\theta_{Az} = 0^\circ$ (up/downwind) curve and the $\theta_{Az} = 90^\circ$ (crosswind) curve.

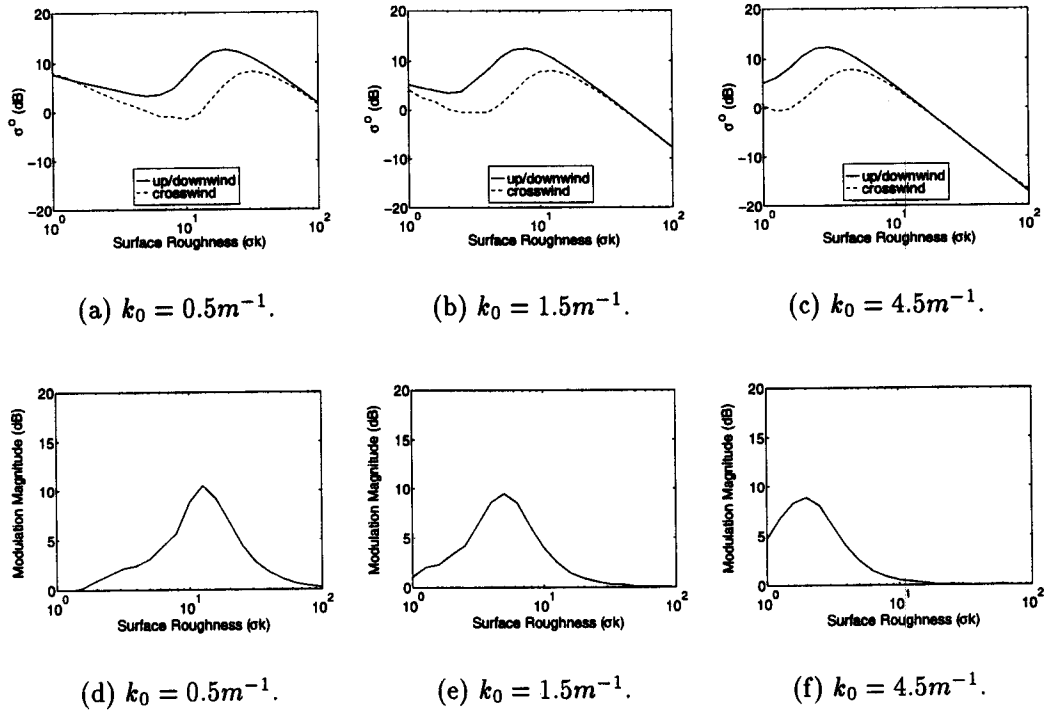


Figure 3.6: Dependence of the modulation on the low wave number cut-off (k_0). The plots were generated using $p = 4.0$, $\theta_0 = 90^\circ$, $\theta_i = 10^\circ$, and $f = 10\text{GHz}$ ($k = 209m^{-1}$). The top row of figures shows σ° for $\theta_{Az} = 0^\circ$ (up/downwind) and $\theta_{Az} = 90^\circ$ (crosswind). The bottom row shows the modulation magnitude, which is the difference between the $\theta_{Az} = 0^\circ$ (up/downwind) curve and the $\theta_{Az} = 90^\circ$ (crosswind) curve.

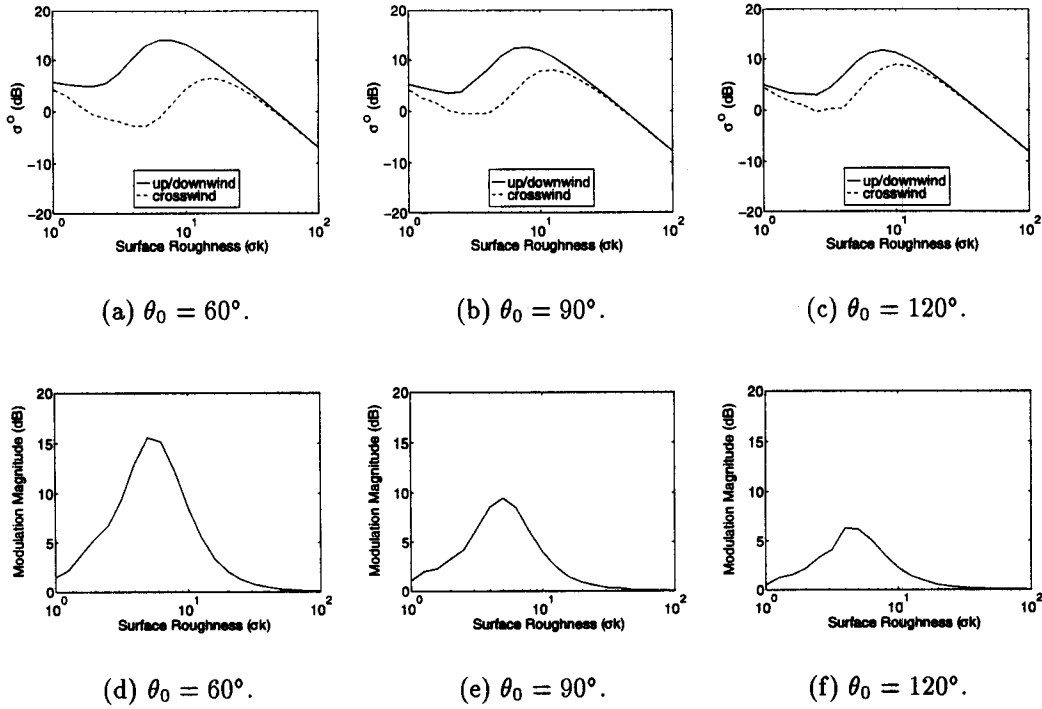


Figure 3.7: Dependence of the modulation on the directional parameter (θ_0 .) The plots were generated using $p = 4.0$, $k_0 = 1.5m^{-1}$, $\theta_i = 10^\circ$, and $f = 10GHz$ ($k = 209m^{-1}$). The top row of figures shows σ^0 for $\theta_{Az} = 0^\circ$ (up/downwind) and $\theta_{Az} = 90^\circ$ (crosswind). The bottom row shows the modulation magnitude, which is the difference between the $\theta_{Az} = 0^\circ$ (up/downwind) curve and the $\theta_{Az} = 90^\circ$ (crosswind) curve.

3.2.3 Dependence on the directional parameter (θ_0)

According to Figure 3.7, the azimuth modulation decreases as θ_0 , the directional parameter, increases. Considering a surface with a roughness of 10, modulations of 8.5, 4, and 2dB are present for θ_0 values of 60° , 90° , and 120° respectively. This trend is correctly explained according to intuition. A surface with a larger θ_0 values has wave energy traveling in more directions. Thus, there are surface facets pointing in more directions, and thus, power is scattered in more directions. The azimuth modulation decreases with increasing θ_0 values.

3.2.4 Dependence on the incidence angle (θ_i)

As shown in Figure 3.8, the azimuth modulation increases with increasing incidence angle (θ_i). According to the figure, for a surface with a roughness of 10, the modulation increases from 1dB to 4dB to 10dB as the incidence angle increases from 5° to 10° to 20° . To understand this trend, consider the example surfaces in Figure 3.9. This figure shows that the contrast in the perpendicular facets for the different azimuth angles is much greater when $\theta_i = 20^\circ$ than when $\theta_i = 10^\circ$. To understand this, consider what is happening as θ_i increases. As θ_i increases, the incident electromagnetic path is becoming more shallow, and the perpendicular facets are becoming steeper. Assuming that the surface is directed, and the perpendicular facets are becoming steeper, the number and size of the perpendicular facets decreases more rapidly in the crosswind case than in the up/downwind case (see also Figures 3.4c and d). Hence, the azimuth modulation increases. For surfaces rougher than that shown in Figure 3.9, the modulation increase is less pronounced, but it remains present.

3.2.5 Dependence on the radar frequency (f)

Finally, the azimuth modulation dependence on frequency is shown in Figure 3.10. The standard deviation of the surface (σ) rather than the surface roughness (σk) is plotted along the horizontal axis in Figure 3.10 so that similar surfaces can be more easily compared. The dependence of the modulation on radar frequency depends also on the roughness of the surface. When σ is small, the peak of the modulation is increased as a function of frequency. However, if $\sigma = 0.0477\text{m}$ (corresponding to a roughness of 10 when $f = 10\text{GHz}$), the modulation is approximately 4dB for all frequencies shown. The modulation decreases slightly as a function of frequency, but the difference between 5.3GHz and 14GHz is less than 1dB. Thus, for practical surfaces, the modulation is predicted to change very little as a function of frequency.

3.3 Summary

Azimuth modulation is predicted at near-normal incidence angles. Directed surfaces give rise to azimuth modulation because there are more facets facing

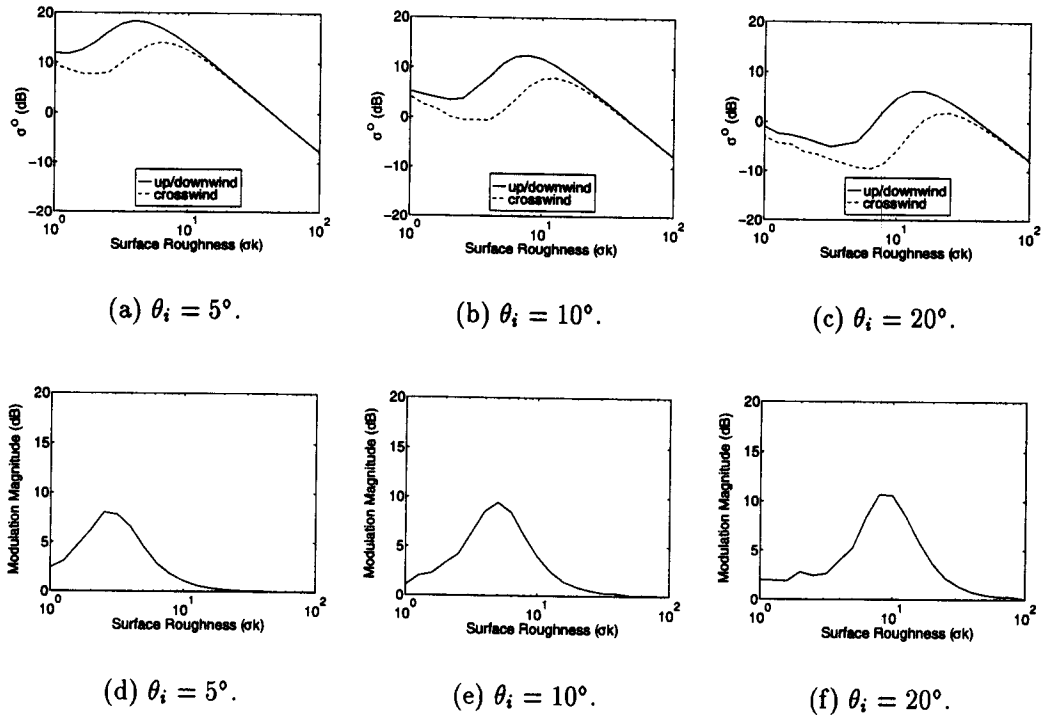


Figure 3.8: Dependence of the modulation on incidence angle (θ_i). The plots were generated using $p = 4.0$, $k_0 = 1.5m^{-1}$, $\theta_0 = 90^\circ$, and $f = 10GHz$ ($k = 209m^{-1}$). The top row of figures shows σ^0 for $\theta_{Az} = 0^\circ$ (up/downwind) and $\theta_{Az} = 90^\circ$ (crosswind). The bottom row shows the modulation magnitude, which is the difference between the $\theta_{Az} = 0^\circ$ (up/downwind) curve and the $\theta_{Az} = 90^\circ$ (crosswind) curve.

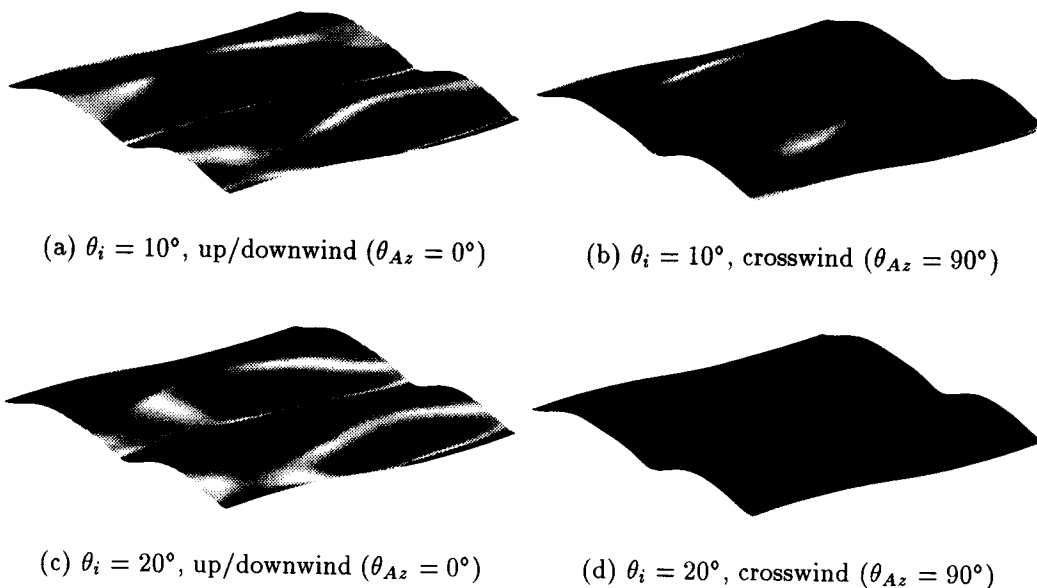


Figure 3.9: Scattering from a rough surface at two incidence angles. The highlighted portions of the surface are the facets that are perpendicular to the incident electromagnetic path. Note the difference in the facets between the up/downwind case and the crosswind case for each surface. There is modulation at 20° than at 10° . The surfaces depicted are $1.28m \times 1.28m$ in size, and the parameters are $\sigma = 0.04m$, $p = 4.0$, $k_0 = 1.5m^{-1}$, and $\theta_0 = 90^\circ$.

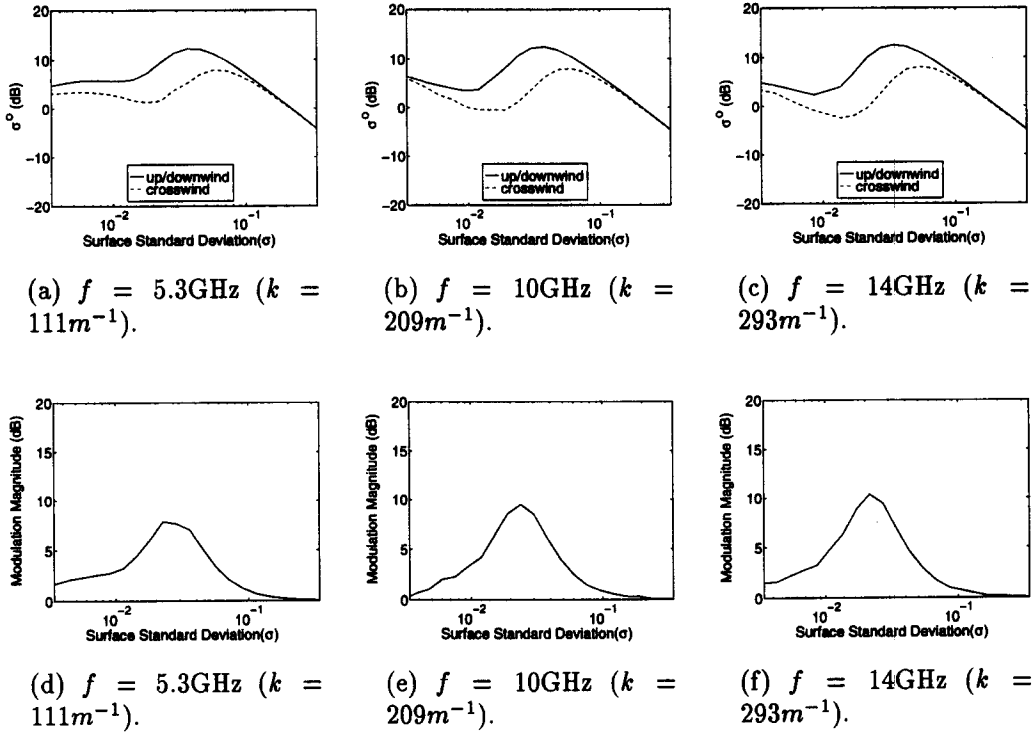


Figure 3.10: Dependence of the modulation on the radar frequency (f). The plots were generated using $p = 4.0$, $k_0 = 1.5\text{m}^{-1}$, $\theta_0 = 90^\circ$, and $\theta_i = 10^\circ$. The top row of figures shows σ° for $\theta_{Az} = 0^\circ$ (up/downwind) and $\theta_{Az} = 90^\circ$ (crosswind). The bottom row shows the modulation magnitude, which is the difference between the $\theta_{Az} = 0^\circ$ (up/downwind) curve and the $\theta_{Az} = 90^\circ$ (crosswind) curve.

some directions than others. For practical surfaces, the modulation decreases as the surface becomes rougher, and it disappears for very rough surfaces. Further, for practical surfaces, the modulation is predicted to increase when the surface power parameter (p) is increased, decrease when the low wave number cut-off (k_0) or the directional parameter (θ_0) are increased, increase when the incidence angle (θ_i) is increased, and vary little with changes in the radar frequency (f). Physically, these trends can be explained in terms of the orientation of the facets on a rough surface.

The orientation of the facets on the surface gives a good physical intuition for the prediction of azimuth modulation of the radar backscatter. However, it has not been shown if the predictions are correct. To gain confidence in the predictions, they must be compared to radar data. If the predictions are correct, the theory can be used to predict azimuth modulation with confidence.

EXPERIMENTAL AZIMUTH MODULATION AT NEAR-NORMAL INCIDENCE

In order to test the performance of the theory, its predictions are compared to radar data. The radar data was generated during an experiment conducted by the Brigham Young University Microwave Earth Remote Sensing (MERS) research group. The main radar system used during the experiment is known as YSCAT, and the experiment is known as the YSCAT94 experiment. The YSCAT radar is an ultra wide band scatterometer and has the capability to operate at frequencies from 2GHz to 18GHz. It also has the capability to scan over a 160° range in azimuth angle and from 0° to greater than 90° in incidence angle (Collyer, 1994). In addition to the YSCAT radar, other sensors were present to measure environmental and surface wave conditions.

The data from the YSCAT radar experiment shows that azimuth modulation is indeed present at near-normal incidence angles. The data also shows that the azimuth modulation decreases as the roughness of the water surface increases, as predicted by the theory.

The YSCAT94 experiment was conducted from May-November, 1994 at the Canada Centre for Inland Waters (CCIW) research tower on Lake Ontario, Canada. A map showing the location of the tower on Lake Ontario is shown in Figure 4.1. As shown on the map, the location of the tower allowed the wave fetch to range from $1km$ to hundreds of kilometers, depending on the wind direction. This allowed for a variety of wave conditions.

4.1 Data Collection

A variety of radars and sensors were deployed in the YSCAT94 experiment. A diagram showing the locations of the various sensors on the tower is shown in Figure 4.2, and a photo of the radar deployment is shown in Figure 4.3. The sensors used for the study in this thesis are the YSCAT radar system, the

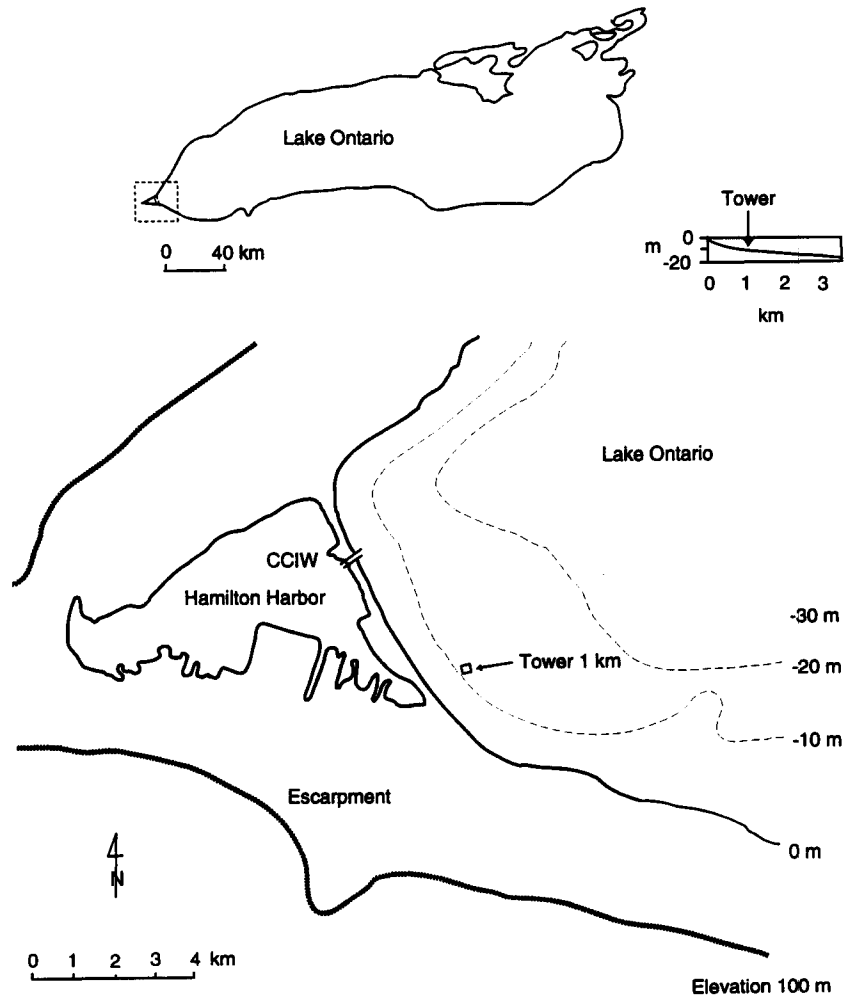


Figure 4.1: Map showing the location of the CCIW Research Tower. From (Collyer, 1994).

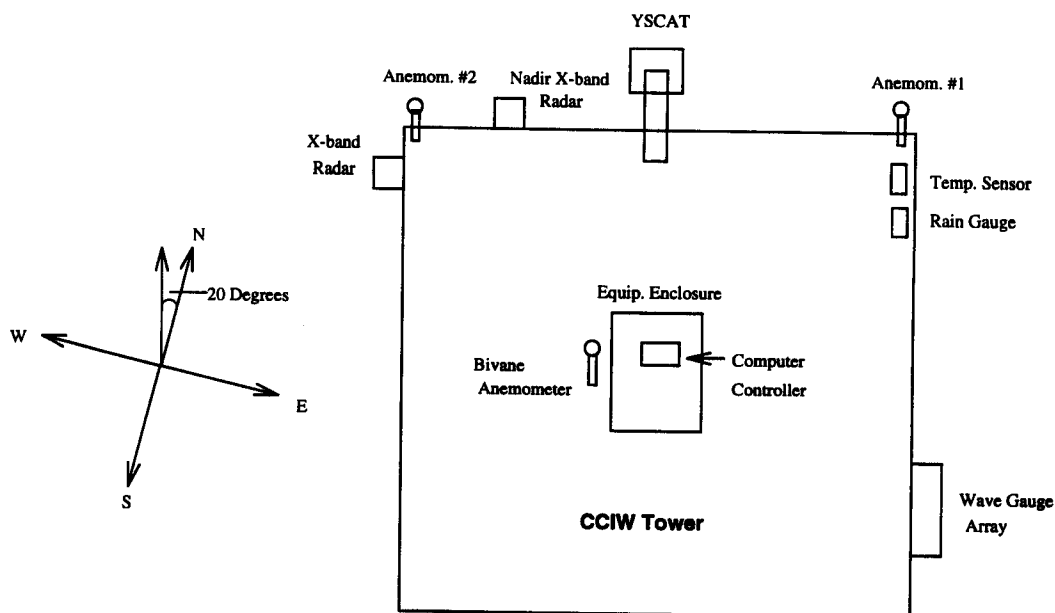


Figure 4.2: Diagram of YSCAT deployment on the CCIW Tower. From (Collyer, 1994).

anemometers, and the wave gauge array.

4.1.1 The YSCAT radar system

The YSCAT radar system was designed in the Microwave Earth Remote Sensing laboratory at Brigham Young University. It had the capability to scan through a 160° range in azimuth angle and from 0° to greater than 90° in incidence angle. It also had the capability to transmit frequencies from 2GHz to 18GHz in either vertical or horizontal polarization modes. It utilized a specially designed elliptical transmit antenna with a nearly constant beamwidth of 5° over the frequency range 4GHz to 18GHz. At 2GHz, the beamwidth approached 8° . YSCAT's receive antenna was a quad-ridge horn with a beamwidth range of 45° to 7.5° over the frequency range of 2GHz to 18GHz.

For the YSCAT94 experiment, YSCAT was mounted on the north side of the CCIW tower 6.26 meters above the water surface. The geometry (see Figure 4.2) was defined such that a radar azimuth angle of 180° corresponded to looking straight out from the tower or to a compass direction of 20° west of north. Looking straight out from the tower was the center of YSCAT's azimuth scan range.

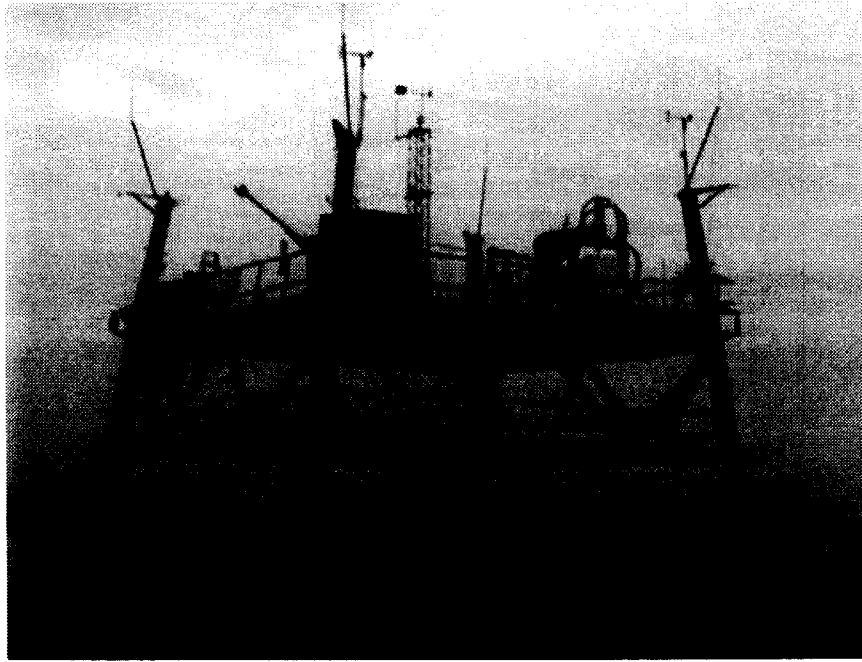


Figure 4.3: Photo of YSCAT deployment on CCIW research tower. From (Collyer, 1994).

The YSCAT system was controlled by a 486 personal computer. The computer took as input a file known as a measurement script, and for versatility, a different script was created for each experimental study of interest. For each measurement in the script, a desired elevation angle, azimuth angle, transmit frequency, and transmit polarization were specified. The computer then adjusted the radar to correspond to the desired parameters and sampled the return power on both horizontally and vertically polarized receive channels. In addition to controlling the radar, the computer also sampled weather data, allowing wind information to be available with the radar data.

4.1.2 YSCAT data collection at near-normal incidence

A measurement script for YSCAT was written specifically for the study described in this thesis. This script requested measurements at near normal incidence angles and vertical polarization, and the measurements were grouped into 5 different azimuth scans. Each azimuth scan consisted of measurements taken at a single transmit frequency and incidence angle. The first two azimuth scans

consisted of measurements taken at a frequency of 5.3GHz; the incidence angles were 10° and 20° respectively. Similarly, the next two scans were at a frequency of 10.02GHz using 10° and 20° respective incidence angles. The last scan was at a frequency of 14GHz and an incidence angle of 10° .

Each azimuth scan requested measurements at 9 different azimuth angles. The first measurement was taken at an azimuth angle of 100° (the lower limit of YSCAT's capability), and each successive measurement incremented the azimuth angle by 20° until an azimuth angle of 260° (the upper limit of YSCAT's capability) was reached. The measurement script then proceeded to the next azimuth scan.

Since the YSCAT radar system was used for a variety of experimental studies, several measurement scripts were grouped into a data collection mode. The script described above was included in YSCAT's azimuth scan mode. YSCAT was operated in azimuth scan mode for 2 to 8 days at a time approximately once every two weeks. When YSCAT was in azimuth scan mode, the script (described above) for this study was executed approximately once every six hours. It took YSCAT about 12.5 minutes to complete each azimuth scan in the script, and about 63 minutes to complete the entire script.

4.1.3 Other experimental sensors

As mentioned previously, in addition to YSCAT, other sensors were deployed on the research tower (see Figure 4.2). Data from these sensors was sampled at 10Hz and stored in 17 minuted data files by a second 486 personal computer. For this study, the quantity of interest from these sensors was the water surface height as a function of time. This quantity was available from one of the wave staffs and was used to estimate the surface low wave number cut-off (k_0) and standard deviation (σ). Knowledge of these parameters was necessary to facilitate comparison between the theory and the radar data.

4.2 Known Measurement Errors

4.2.1 Azimuth slip

There are two known irregularities in the data collection of the radar deployment. First, as the radar experiment progressed, a failure was detected in the radar azimuth encoding system. This failure caused the system to slip over time, creating errors in the positioning of the radar azimuth. The amount of slip is known over time, and the radar azimuth angles used for data analysis have corrected using a matlab routine provided by Ryan Reed. The routine corrects the measured azimuth angle based on the time the measurement.

4.2.2 Clock drift

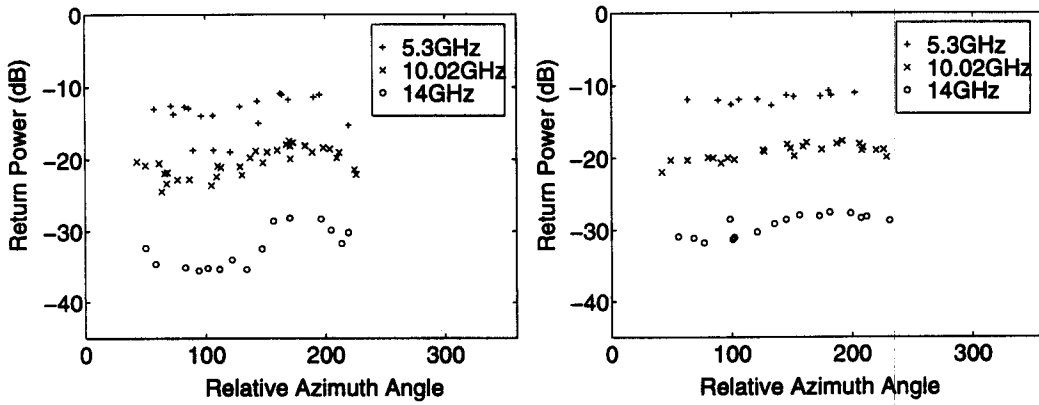
The other known problem has to do with computer clock drift. Over a time period of approximately one month, the YSCAT computer clock would typically run slow by approximately 10 minutes. In the same time period, the clock in the 486 personal computer collecting data from the other sensors typically ran fast by approximately 20 minutes. Other time errors occurred intermittently and were caused by operator errors such as setting the date on one of the computers incorrectly. It was necessary to quantify these errors to gain confidence that the surface data from the wave gauge array was taken at approximately the same time as radar data was taken by the YSCAT computer.

Because the YSCAT computer sampled data from anemometers #1 and #2 (see Figure 4.2) and the other computer sampled the bivane anemometer, wind speed data was used as the basis for quantifying clock errors. The clock error was found once each day by forming wind speed data from both computers into vectors. The vectors were time-shifted with respect to each other, and the mean-squared error and correlation were computed. The time shift for which the two vectors were most nearly the same was taken as an estimate of the clock error. It was insured that the estimates on successive days were consistent with the expected clock drift. The procedure allowed time corrections to within a few minutes, which was acceptable for the purposes of this study.

4.3 Comparison of Experimental Results to Theory.

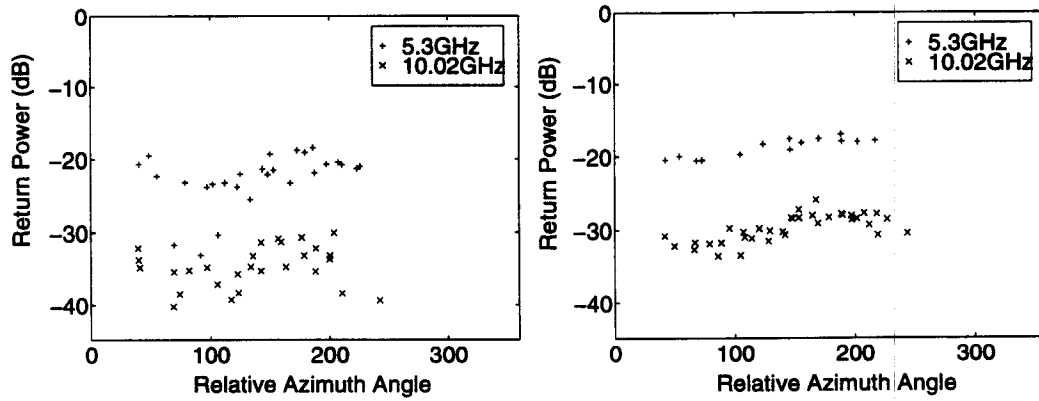
Figure 4.4 shows some representative results from data gathered at the YSCAT radar experiment as described Section 4.1.2. The data in the figure were gathered between July 20, 1994 and July 22, 1994. This data verifies the presence of azimuth modulation at near-normal incidence angles. Notice that the azimuth modulation decreases when the wind speed increases. Since in general the roughness of the surface increases when the wind speed increases, verifies the general trend that the modulation decreases with increasing surface roughness. As predicted by the theory, the modulation in the data is increasing with increasing incidence angles, although some of this increase is obscured by variability in the data. The modulation is further increasing with increasing radar frequency. While this was not predicted by the theory, the lack of this trend in the theory is attributed to the simplicity of the surface model used. In particular, it is not known how the directionality of the surface may vary as a function of the wave number on the surface. In the model used herein, the directionality was assumed to be independent of surface wave number. If the directionality is modeled as function of surface wave number, a dependence based on frequency such as has been observed is a likely result. The preliminary results in Figure 4.4 indicated that the theory is worth pursuing to explain azimuth modulation, although the frequency dependence is seen to be incorrect.

To investigate the theory, it was compared to the data in two ways. First, a few representative azimuth scans were chosen. For each scan, the relative normalized radar cross-section was plotted as a function of azimuth angle. A theoretical curve was calculated and plotted on the same axes. This allowed the shape of the modulation curve and the magnitude of the modulation to be verified for some specific cases. Then, the modulation magnitude was found for all of the azimuth scans. This modulation magnitude was plotted as a function of the surface standard deviation (σ) which is proportional to the surface roughness. This allowed the trend of the modulation magnitude as a function of surface roughness to be verified.



(a) $\theta_i = 10^\circ$, wind between 3 and 5m/s

(b) $\theta_i = 10^\circ$, wind between 6 and 10m/s



(c) $\theta_i = 20^\circ$, wind between 3 and 5m/s

(d) $\theta_i = 20^\circ$, wind between 6 and 10m/s

Figure 4.4: Empirical results from data gathered at the YSCAT experiment. The data were gathered from July 20 through July 22, 1994.

4.3.1 General data processing

For all of the comparisons of the theory to data, estimates of the low wave number cut-off (k_0) and the surface standard deviation (σ) were needed. These parameters were estimated by considering the water surface height data from the wave staff array. Separate estimates were formed to correspond to each azimuth scan completed by YSCAT. The first step in the estimation was to identify the wave staff data file whose start time was closest to the start time of the azimuth scan in question. To find the correct file, it was necessary to correct for computer clock drift as described in the Section 4.2.2. Once the correct file was identified, the spectrum of the output of one wave staff was then computed by segmenting the samples in the file into records of length 300 points (30 seconds). Adjoining records overlapped by 100 points. A periodogram was then computed for each record, and the periodograms were averaged, giving an estimate of the wave spectrum as a function of (time) frequency. The frequency axis was converted to wave numbers using the approximation (valid for long, gravity waves) $\omega^2 = gk_w$ where ω is the radian frequency, g is the acceleration of gravity ($g = 9.81ms^{-2}$), and k_w is the water wave number.

As discussed previously in Section 2.1.2, the waves of interest were those with heights on the order of one electromagnetic wavelength. These waves were observed to be those with wavenumbers on the order of $k_w = 1.5m^{-1}$. Thus, the part of the spectrum considered in the estimation process was limited to wavenumbers k_w such that $k_w \geq 1.43m^{-1}$. The actual cut-off was arbitrary, and it was observed that small changes made little difference. It was also observed that for large values of k_w , the signal to noise ratio in the spectral estimate was unacceptably small. However, it was possible to estimate the required parameters using only smaller k_w values where the signal to noise ratio was acceptable. Thus, the noisy part of the spectrum was identified and discarded. The maximum value of the remaining part of the power spectrum was taken to be the low wave number cut-off, k_0 . The spectrum was then integrated over $k_w > k_0$ to estimate the variance, σ^2 . The standard deviation (σ) was then found by taking the square root of the variance.

4.3.2 Relative normalized radar cross-section vs. azimuth angle

The first comparison of the theory to the data was to plot the normalized radar cross-section (proportional to return power) is plotted as a function of azimuth angle. To facilitate comparison to the theory, data from only one azimuth scan was included in a single plot. The low wave number cut-off (k_0) and surface standard deviation (σ) corresponding to the plotted scan were estimated from wave staff data as described in Section 4.3.1. Measurements to reliably estimate the power parameter (p) and the directional parameter (θ_0) were lacking, so $p = 4.0$ and $\theta_0 = 90^\circ$ were assumed. These are reasonable values which are consistent with known observations (Donelan and Pierson, 1987). Since the radar incidence angle and frequency were known, the theory could be used to generate an expected curve. The theory and data were compared by plotting them on the same set of axes. During this study, absolute calibration data was not available for the YSCAT radar system, so the relative normalized radar cross section (normalized radar cross section with the mean removed from the data) was plotted.

Figures 4.5 and 4.6 show examples of the normalized radar cross-section plotted as a function of relative azimuth angle. Figure 4.5 shows an example when the modulation is high, and Figure 4.6 provides an example when the modulation is low. Precision problems with numerical integration are responsible for the bumps on the theory curves in the figures.

Examination of the figures shows that many of the modulation trends are correctly predicted. For example, the theory correctly predicts that the modulation decreases when the surface roughness increases. Comparison of Figure 4.5 with Figure 4.6 shows that the amount of the modulation decrease is approximately correct. In addition to predicting the decrease in modulation as a function of surface roughness, the figures also show that the theory predicts the correct shape for the modulation curve. This shape looks similar to a cosine wave, as noted in the preliminary results.

As previously mentioned, the theory does not predict the modulation to change as a function of frequency. However, the modulation in the data is increasing with increasing frequency, particularly when the surface roughness is low (and the modulation is high). Thus, the modulation magnitude is predicted

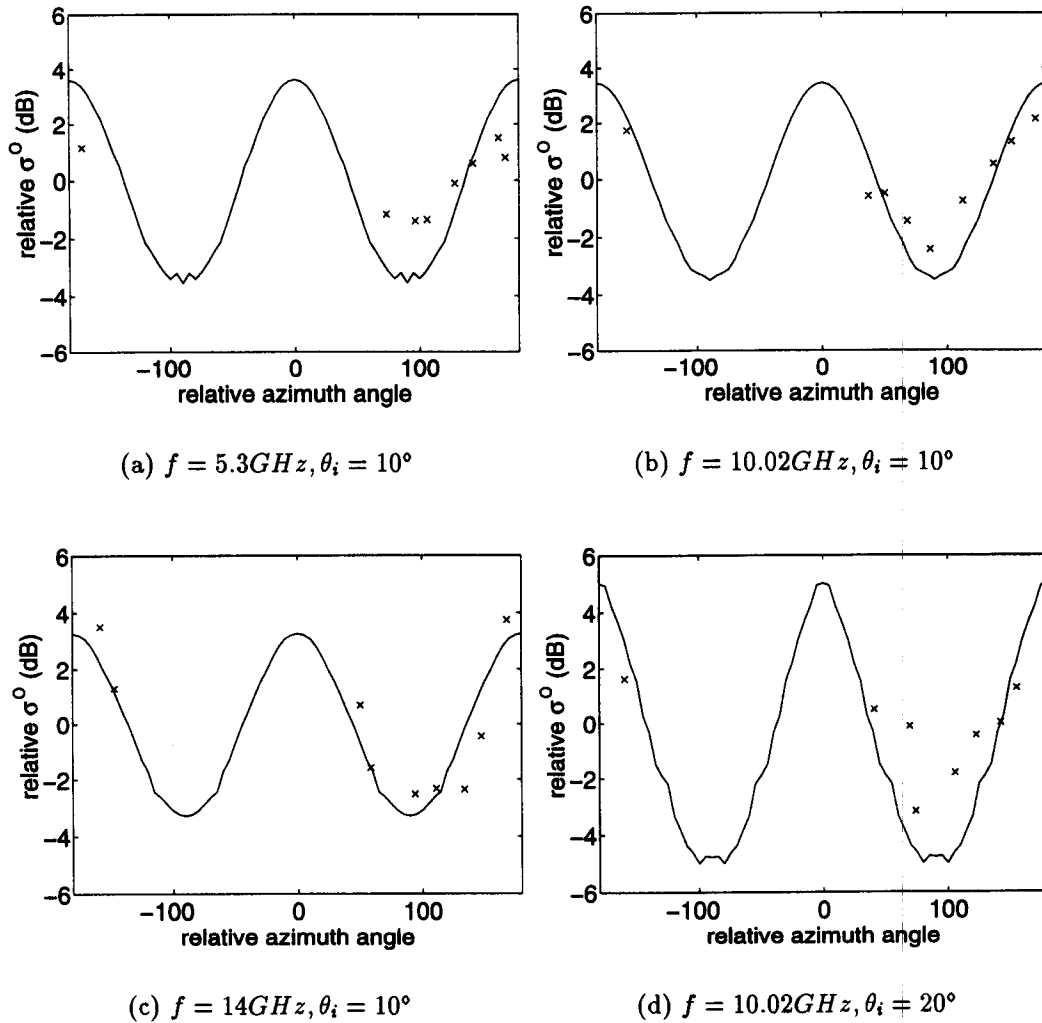


Figure 4.5: Relative σ° (small surface roughness): Comparison of measured values to theoretical values. The measured value of the surface standard deviation (σ) was 0.0369, and the measured value of k_0 was 1.43. The theoretical plots were generated with $\sigma = 0.0369$, $k_0 = 1.43$, $p = 4.0$, and $\theta_0 = 90^\circ$.

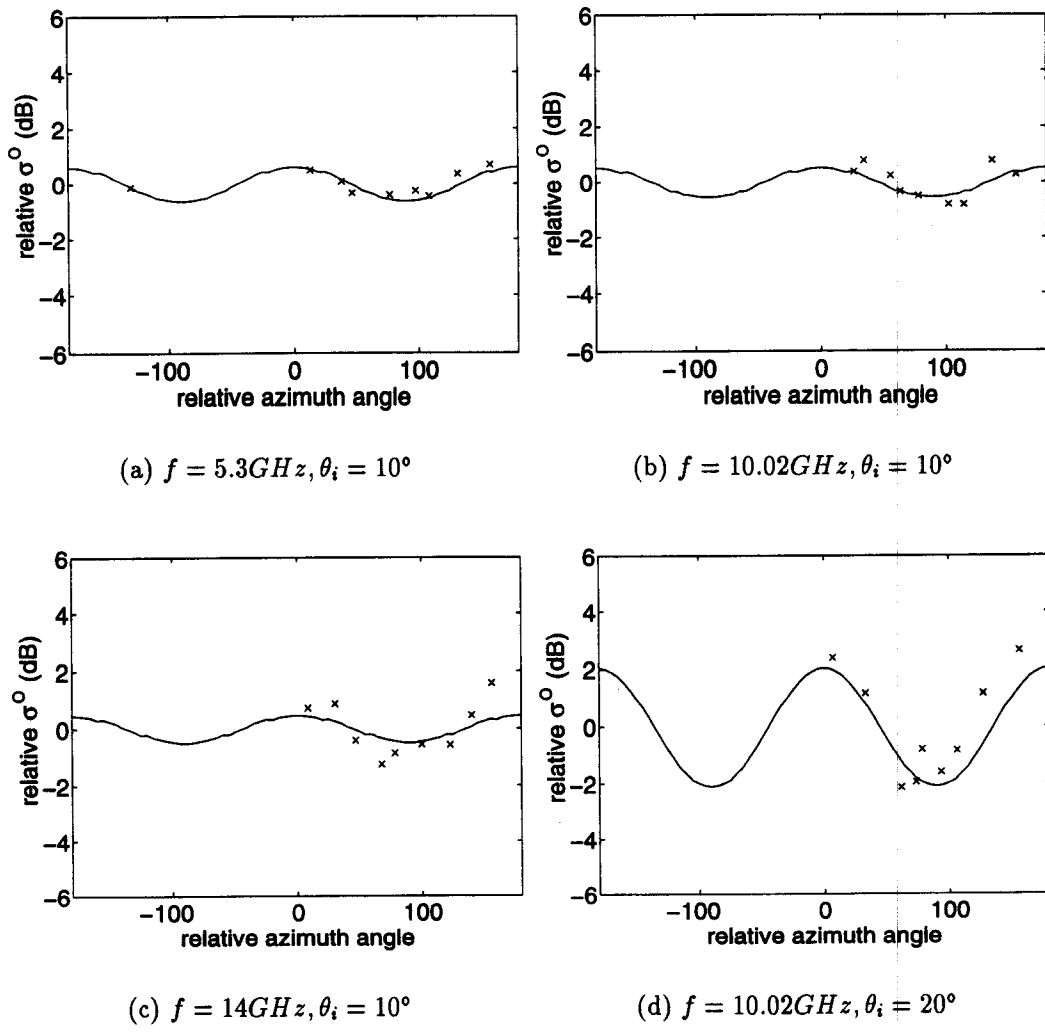


Figure 4.6: Relative σ^0 (large surface roughness): comparison of measured values to theoretical values. The measured value of the surface standard deviation (σ) was 0.0939, and the measured value of k_0 was 1.43. The theoretical plots were generated with $\sigma = 0.0939, k_0 = 1.43, p = 4.0,$ and $\theta_0 = 90^\circ$.

to be larger than observed in the data at 5.3GHz and smaller than observed in the data at 14GHz. The data also shows that there is some modulation dependence on frequency when the surface roughness is high and the modulation is low (see Figure 4.6). However, in this case the dependence is smaller; thus, the prediction error is also much smaller. As noted previously, the lack of modulation dependence on frequency in the theory is likely the result of the simplifications made to the surface model. The prediction is likely to be corrected considering a directional dependence on wave number in the power spectral density model.

After examining the (relative) normalized radar cross-section as a function of azimuth angle, it appears that in general, the theory is better at predicting azimuth modulation when the surface roughness is large. Although this was not initially expected, it can be explained in terms of the surface model. When the surface roughness large, the power spectral density most nearly fits the model. In contrast, when the roughness of the surfaces is low, the wind speed is usually low as well. When the wind is low the wind direction is highly variable, making the surface appear to be more isotropic. This leads to less azimuth modulation than expected. In addition, when the wind is low, non-local or residual surface effects may be present. This leads to a spectral shape that does not fit the k^{-p} model. This, too, leads to theoretical results that do not fit data.

4.3.3 Modulation magnitude vs. roughness

The second comparison of the theory to the data was to plot the modulation magnitude as a function of surface standard deviation or roughness. As before, k_0 and σ were estimated for each scan; $p = 4.0$ and $\theta_0 = 90^\circ$ were assumed; and the radar frequency and incidence angle were known. Thus, a theoretical modulation magnitude could be computed for each scan.

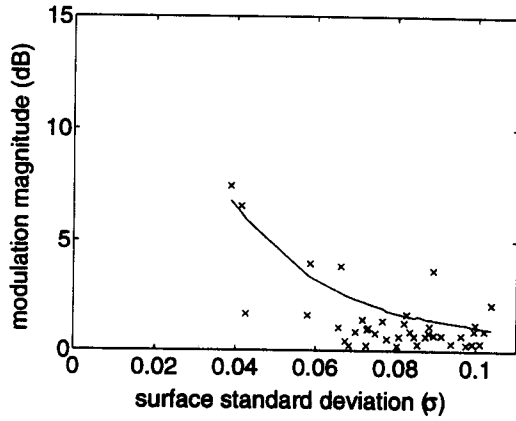
To plot the data points, an estimate of the modulation magnitude given the data from a radar azimuth scan was required. This estimate was formed by fitting the function $A \cos(2\theta_{Az} + \phi) + B$ to the return power (in dB) points from a single radar azimuth scan and taking $2A$ as the estimated modulation magnitude. The cosine function was chosen because the azimuth modulation curves (see Figure 4.4 resembled a cosine in shape. The variance of the fit was computed for each

scan, and scans for which this variance exceeded $0.5A$ were discarded. These scans were discarded because in general, they corresponded to surface conditions that did not fit the k_w^{-p} power spectral density model. Thus, the data from scans did not resemble a cosine in shape leading to a large variance in the fit and unreliable modulation information.

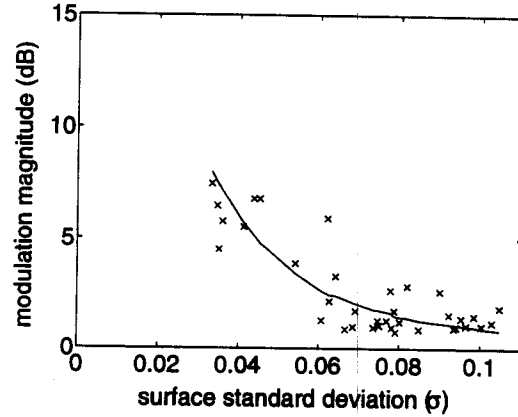
Figure 4.7 shows some of the plots of modulation magnitude as a function of surface roughness. The measured points in Figure 4.7 represent scans for which $k_0 = 1.43m^{-1}$. The data in the plots appear to have a large scatter, particularly at 20° incidence, making some trends difficult to identify. However, the fits of the theory to the data have been quantified by computing the mean squared error between the data and the theory and dividing by the variance of the data. Subtracting this parameter from unity gives a measure of the quality of the fit. This measure gives the percentage of the variability in the data that is explained by the theory.

When the incidence angle is 10° , 35% of the variability is explained at 5.3GHz, 71% at 10.02GHz, and 65% at 14GHz. Thus, the theory fits best at 10.02GHz. The fit is nearly as good at 14GHz, but its quality is diminished at 5.3GHz. From the figure, it can be seen that too much modulation is consistently predicted at 5.3GHz, leading to the low fit parameter. As previously discussed, the simplifications in the model limit its prediction of the modulation trend as a function of frequency. Thus, the model can be tuned to fit the data at one frequency by choosing an appropriate value of θ_0 , but this will limit its fit at other frequencies.

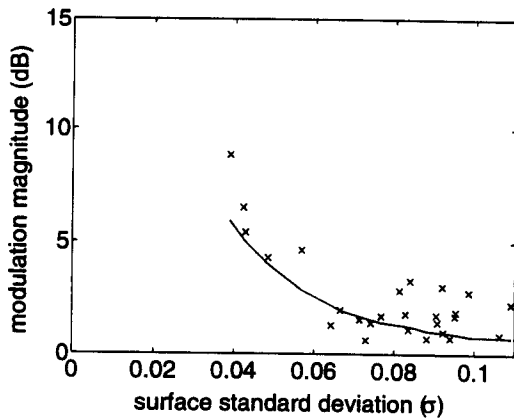
When the incidence angle is 20° , the quality of the data fit is poor such that computing fit parameter resulted in a value that did not make sense. In fact, using Figure 4.7, it is difficult to see that the modulation increases with increasing incidence angle. However, Figure 4.8 shows that this is indeed the case by plotting the ratio of the modulation magnitudes for 10° and 20° scans that were taken immediately following each other. Notice that the ratio of the 20° scan to the 10° scan is nearly always larger than unity. Referring back to Figure 4.7, the predicted increase in modulation as a function of incidence angle is more than the actual increase. However, the variability in the 20° data is so high that some of the



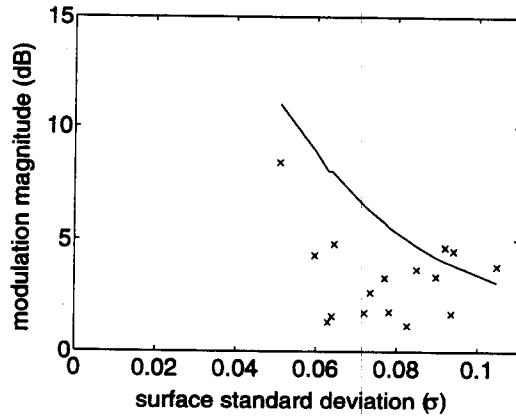
(a) $f = 5.3GHz, \theta_i = 10^\circ$



(b) $f = 10.02GHz, \theta_i = 10^\circ$



(c) $f = 14GHz, \theta_i = 10^\circ$



(d) $f = 10.02GHz, \theta_i = 20^\circ$

Figure 4.7: Comparison of measured values of the modulation magnitude to theoretical values as a function of surface standard deviation (σ). All of the measured points shown have a corresponding measured $k_0 = 1.43^{-1}$. The theoretical points were generated with $k_0 = 1.43m^{-1}$, $p = 4.0$, $\theta_0 = 90^\circ$, and σ values to match those corresponding to the measured points. Numerical problems are responsible for the bumps on the theory curves.

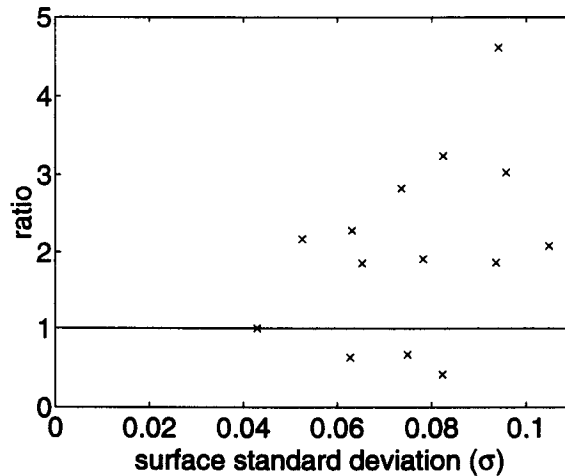


Figure 4.8: Ratio of measured modulation magnitude at $\theta_i = 20^\circ$ to measured modulation magnitude at $\theta_i = 10^\circ$. The radar frequency was 10.02GHz, and the 20° scans were taken immediately following the 10° scans.

increase in modulation may be masked, particularly when the surface roughness is low. The error in predicting the modulation at 20° is largest when the surface roughness is small. Thus, as found previously, the theory works best when the surface roughness is high.

4.4 Summary

The theory was tested by comparing it to data taken by the YSCAT radar system on Lake Ontario, Canada. The trend of decreasing modulation as the surface roughness increases was verified. The shape of the modulation curve as a function of azimuth angle was also verified. However, there are problems predicting the frequency dependence of the modulation. These problems are likely the result of an over simplified surface model. In particular, if the directionality of the surface is a function of the wave number, the frequency dependence is likely to be explained. There are also problems with the incidence angle dependence of the modulation. However, the extent of these problems is unknown because there are also problems with the radar data at 20° incidence angle. More experimentation is needed to clarify the incidence angle trend.

By comparing the theory to radar data, confidence has been gained in its predictions. The most prevalent trend observed is the decrease in azimuth

modulation as the surface roughness increases. This prevalent trend, along with shape of the modulation curve has been correctly predicted. Since these trends are correctly predicted, the theory can be used to infer information about a random surface. Thus, the theory has contributed to the understanding of radar backscatter at near-normal incidence.

CONCLUSIONS

In the past, it has often been assumed that there is no azimuth modulation of the radar backscatter at near-normal incidence. However, the YSCAT94 radar experiment shows between 0 and 10 dB of modulation at 10° incidence angle. Thus, there is a need to understand the physical causes of the modulation and the effects of the surface and radar parameters on the modulation. The theory derived in this thesis predicts the shape of the modulation curve (the normalized radar cross-section plotted as a function of incidence angle), and it correctly predicts the modulation decrease as a function of surface roughness. It has problems predicting the modulation change as a function of the radar frequency, but this could likely be corrected by allowing dependence of the directionality of the surface on wave number. The model also appears to have problems predicting the magnitude of the modulation change as a function of incidence angle (although the trend is correctly predicted), but more experimentation is needed to clarify this trend.

5.1 Contributions

It the past, it has sometimes been assumed that the near-normal radar backscatter exhibits little or no azimuth dependence (Colton, 1989). Thus, more observations and understanding relating to near-normal azimuth modulation are needed. The theory in this thesis has been derived and studied to develop such understanding. The derivation begins by modeling the ocean surface as a two-dimensional stochastic process. The surface model includes the following assumptions:

1. The surface statistics are Gaussian.
2. The power spectrum has a $k_w^{-p} u(k_w - k_0)$ wave number dependence
3. The power spectrum has a $\exp\left[-3\left(\frac{\theta - \theta_{Az}}{\theta_0}\right)^2\right]$ directional dependence
4. The directional dependence is independent of wave number.

This surface model allows the electromagnetic backscatter to be computed using Green's theorem and a physical optics approach. In addition to the assumptions about the surface, the derivation requires the following assumptions about the radar system:

1. The electromagnetic wave is time-harmonic
2. The ocean surface is in the far-field of the antenna
3. The electromagnetic wavelength is much smaller than the radius of surface curvature

The third assumption is necessary to insure that the tangent plane or physical optics approximation applies. The result of the derivation is the backscatter integral (Equation 2.27), the basis for predicting the normalized radar cross-section and hence the azimuth modulation.

A directed ocean surface leads to azimuth modulation of the radar backscatter. The modulation can be explained physically in terms of the orientation of surface facets in different azimuth directions. The magnitude of the modulation is a function of the surface parameters (σ , k_0 , p , and θ_0) and the radar parameters (θ_i , and f). The expected trends with respect to these parameters are explained in terms of their effects on the areas of the surface that are perpendicular to the incident electromagnetic path.

To verify the theory, it is compared to data from the YSCAT94 radar experiment. As mentioned above, azimuth modulation of the radar backscatter at near-normal incidence is observed in the YSCAT data. By programming YSCAT to take data at several successive azimuth angles, it is possible to construct a plot of the normalized radar cross-section as a function of radar azimuth angle. The surface parameters relating the plot are estimated, and a theory plot is constructed. The shape of the theoretical curve is found to agree well with the shape of the data curve. At a frequency of 10.02GHz and an incidence angle of 10° , the theoretical modulation magnitude also agrees well with the data. By plotting the modulation magnitude in the data as a function of the surface roughness and comparing it to theory, it is also found that the theory correctly predicts that the modulation will

decrease as the surface becomes increasingly rough. However, the theory consistently predicts too much modulation at 5.3GHz and too little at 14GHz. Thus, the theory does not predict the correct modulation trend as a function of frequency. If the assumption that the directional dependence of the surface spectrum is independent of wave number is relaxed, the prediction of the modulation trend as a function of frequency is likely to be improved. The theory also appears to predict too much modulation at 20° incidence angle. However, because of variability in the data, more experimentation is needed to understand this trend.

5.2 Extensions

Perhaps the most significant extension of this work is to relax the assumption that the directionality of the surface spectrum is independent of the surface wavenumber. This requires quantitative understanding of the dependence of the directionality on the wave number. Significant experimentation may be necessary to develop such an understanding [see (Komen et al., 1994)]. In addition, difficulty is likely to be encountered in deriving the correlation coefficient from this more complicated power spectral density model. Significant numerical modeling is likely to be necessary to do so. If these difficulties can be overcome, however, it may be possible to extend the theory to predict the correct modulation trend as a function of radar frequency.

More experimentation is also needed to understand the dependence of the modulation on incidence angle. It is likely that experimentation in a controlled laboratory environment will help to develop understanding of this trend. Controlled experimentation could lead to the identification of the source of the variability in the data, or it could lead to additional physical information to be included in the model.

Perhaps one more significant extension is to discard the assumption that the surface statistics are Gaussian. The assumption of Gaussian statistics simplifies many of the calculations, but because the troughs of ocean waves are known to be more rounded than the crests, it is not strictly correct. Using a more accurate statistical distribution, it may be possible to predict the difference between upwind and downwind backscatter. As understanding of ocean dynamics improves, better

and better scattering models can be developed. As this happens, it will be possible to better predict azimuth modulation as well.

BIBLIOGRAPHY

- Arfken, G., *Mathematical Methods for Physicists*. Academic Press, Inc., Orlando, FL, 1985.
- Arnold, D. V., *Electromagnetic Bias in Radar Altimetry at Microwave Frequencies*. Ph.D. thesis, Massachusetts Institute of Technology, Cambridge, MA, 1992.
- Banner, M. L., I. S. F. Jones, and J. C. Trinder, "Wavenumber Spectra of Short Gravity Waves." *Journal of Fluid Mechanics*, vol. 198, pp. 321-344, 1989.
- Collyer, R. S., *Dependence of the Normalized Radar Cross Section of Ocean Waves on Bragg Wavelength-Wind Speed and Direction Sensitivity*. Master's thesis, Brigham Young University, Provo, UT, 1994.
- Colton, M. C., *Dependence of Radar Backscatter on the Energetics of the Air-Sea Interface*. Ph.D. thesis, Naval Postgraduate School, Monterey, California, 1989.
- Donelan, M. A., J. Hamilton, and W. H. Hui, "Directional Spectra of Wind Generated Waves." *Phil. Trans. R. Soc. Lond. A*, vol. 315, pp. 509-562, 1983.
- Donelan, M. A. and W. J. Pierson, "Radar Scattering and Equilibrium Ranges in Wind-Generated Waves With Application to Scatterometry." *Journal of Geophysical Research*, vol. 92, no. C5, pp. 4971-5029, 1987.
- Gray, R. M. and L. D. Davisson, *Random Processes: A Mathematical Approach for Engineers*. Prentice-Hall, Inc., Englewood Cliffs, NJ, 1986.
- Jahne, B. and K. S. Riemer, "Two-Dimensional Wave Number Spectra of Small-Scale Water Surface Waves." *Journal of Geophysical Research*, vol. 95, pp. 11531-11546, 1990.
- Johnson, P. E., *Backscatter Sensitivity to the Parameters of a Two-Dimensional Scattering Model*. Master's thesis, Brigham Young University, Provo, UT, 1994.

- Komen, G. J., L. Cavaleri, M. Donelan, K. Hasselmann, S. Hasselmann, and P. A. E. M. Janssen, *Dynamics and Modelling of Ocean Waves*. Cambridge University Press, Cambridge, Great Britain, 1994.
- Kong, J. A., *Electromagnetic Wave Theory*. John Wiley and Sons, Inc., Newyork, NY, 1990.
- Papoulis, A., *Probability, Random Variables, and Stochastic Processes*. McGraw-Hill, Inc., New York, NY, 1991.
- Phillips, O., *The Dynamics of the Upper Ocean*. The University Press, Cambridge, Great Britain, 1966.
- Shemdin, O. H., H. M. Tran, and S. C. Wu, "Directional Measurement of Short Ocean Waves with Stereophotography." *Journal of Geophysical Research*, vol. 93, pp. 13891-13901, 1988.

Appendix A

DERIVATION OF CORRELATION COEFFICIENT

To derive the correlation coefficient, recall from Equations 2.4 and 2.5 that

$$C_p(\rho, \phi) = S_0 \int_{\theta_{Az}-\frac{\pi}{2}}^{\theta_{Az}+\frac{\pi}{2}} d\theta \exp \left[-3 \left(\frac{\theta - \theta_{Az}}{\theta_0} \right)^2 \right] \int_{k_0}^{\infty} dk_w k_w^{-p+1} \cos(k_w \rho |\cos(\theta - \phi)|). \quad (\text{A.1})$$

where S_0 is given by

$$S_0 = \frac{(p-2)k_0^{p-2}}{\frac{\pi}{3}\theta_0 \text{erf}\left(\frac{\sqrt{3}\pi}{2\theta_0}\right)}. \quad (\text{A.2})$$

To simplify the derivation, let $z = \rho |\cos(\theta - \phi)|$ resulting in

$$\int_{k_0}^{\infty} dk_w k_w^{-p+1} \cos(k_w z) \quad (\text{A.3})$$

for the inner integral. This integral can be simplified using Euler's identity, resulting in

$$\frac{1}{2} \int_{k_0}^{\infty} dk_w k_w^{-p+1} e^{ik_w z} + \frac{1}{2} \int_{k_0}^{\infty} dk_w k_w^{-p+1} e^{-ik_w z}. \quad (\text{A.4})$$

These two integrals can in turn be simplified by letting $t = -ik_w z$ and $t = ik_w z$ respectively. Thus,

$$\frac{(-iz)^{p-2}}{2} \int_{-izk_0}^{\infty} dt t^{-p+1} e^{-t} + \frac{(iz)^{p-2}}{2} \int_{izk_0}^{\infty} dt t^{-p+1} e^{-t}. \quad (\text{A.5})$$

The commonly tabulated gamma function is defined by

$$\Gamma(a) = \int_0^{\infty} dt t^{a-1} e^{-t}, \quad \Re\{a\} > 0. \quad (\text{A.6})$$

The restriction on a is necessary to avoid divergence of the integral. For $\Re\{a\} < 0$, the integral definition of the gamma function is not valid, and the gamma function is defined by the Euler infinite limit definition (Arfken, 1985, p. 539). When $\Re\{a\} > 0$, both definitions are equivalent (Arfken, 1985, pp. 540-541). Note that the gamma function obeys the property $\Gamma(a+1) = a\Gamma(a)$ with no restriction on the

argument. When the integral definition is valid, the incomplete gamma function, is defined by

$$\gamma(a, x) = \int_0^x dt t^{a-1} e^{-t}, \Re\{a\} > 0. \quad (\text{A.7})$$

Thus,

$$\int_x^\infty dt t^{a-1} e^{-t} = \Gamma(a) - \gamma(a, x), \Re\{a\} > 0. \quad (\text{A.8})$$

If x is “small”, the incomplete gamma function can be expanded in a Taylor series. The Taylor series can then be used to evaluate an integral of the form $\int_x^\infty dt t^{a-1} e^{-t}$, $\Re\{a\} > 0$.

$$\int_x^\infty dt t^{a-1} e^{-t} = \Gamma(a) - x^a \sum_{r=0}^{\infty} \frac{(-1)^r x^r}{r!(a+r)}, \Re\{a\} > 0 \quad (\text{A.9})$$

(Arfken, 1985, p. 566). The integrals in Equation A.5 look similar to the integral in Equation A.9, but to apply Equation A.9 to Equation A.5 requires that $a = 2 - p$ which does not satisfy the restriction $\Re\{a\} > 0$. However, it can be shown that

$$\int_x^\infty dt t^{a-1} e^{-t} = \Gamma(a) - x^a \sum_{r=0}^{\infty} \frac{(-1)^r x^r}{r!(a+r)}, \forall a \neq 0, -1, -2, \dots \quad (\text{A.10})$$

To see this, first note that Equation A.9 shows that Equation A.10 is true for $\Re\{a\} > 0$. In particular, Equation A.10 holds for $0 < a < 1$. Suppose then that Equation A.10 holds for $n - 1 < a < n$ where n is an integer. Then, let $n - 2 < a < n - 1$ so that $n - 1 < a + 1 < n$.

$$\begin{aligned} \int_x^\infty dt t^{a-1} e^{-t} &= e^{-t} \frac{t^a}{a} \Big|_x^\infty + \frac{1}{a} \int_x^\infty dt t^{(a+1)-1} e^{-t} \\ &= -\frac{x^a}{a} e^{-x} + \frac{1}{a} \left(\Gamma(a+1) - x^{a+1} \sum_{r=0}^{\infty} \frac{(-1)^r x^r}{r!(a+r+1)} \right) \\ &= \Gamma(a) - \frac{x^a}{a} \left(e^{-x} + x \sum_{r=0}^{\infty} \frac{(-1)^r x^r}{r!(a+r+1)} \right) \\ &= \Gamma(a) - \frac{x^a}{a} \left(\sum_{r=0}^{\infty} \frac{(-1)^r x^r}{r!} + \sum_{r=0}^{\infty} \frac{(-1)^r x^{r+1}}{r!(a+r+1)} \right) \\ &= \Gamma(a) - \frac{x^a}{a} \left(1 + \sum_{r=0}^{\infty} \frac{(-1)^{r+1} x^{r+1}}{(r+1)!} + \sum_{r=0}^{\infty} \frac{(-1)^r x^{r+1}}{r!(a+r+1)} \right) \\ &= \Gamma(a) - \frac{x^a}{a} \left(1 + \sum_{r=0}^{\infty} (-1)^r x^{r+1} \left[\frac{1}{r!(a+r+1)} - \frac{1}{r!(r+1)} \right] \right) \\ &= \Gamma(a) - \frac{x^a}{a} \left(1 - a \sum_{r=0}^{\infty} \frac{(-1)^{r+1} x^{r+1}}{(r+1)!(a+r+1)} \right) \end{aligned}$$

$$\begin{aligned}
&= \Gamma(a) - \frac{x^a}{a} \left(1 + a \sum_{r=1}^{\infty} \frac{(-1)^r x^r}{r!(a+r)} \right) \\
&= \Gamma(a) - x^a \sum_{r=0}^{\infty} \frac{(-1)^r x^r}{r!(a+r)}. \tag{A.11}
\end{aligned}$$

This establishes Equation A.10.

Using Equation A.10 in Equation A.5 yields

$$\begin{aligned}
\int_{k_0}^{\infty} dk_w k_w^{-p+1} \cos(k_w z) &= \frac{(-iz)^{p-2}}{2} \left[\Gamma(2-p) - (-izk_0)^{2-p} \sum_{r=0}^{\infty} \frac{(-1)^r (-izk_0)^r}{r!(2-p+r)} \right] \\
&\quad + \frac{(iz)^{p-2}}{2} \left[\Gamma(2-p) - (izk_0)^{2-p} \sum_{r=0}^{\infty} \frac{(-1)^r (izk_0)^r}{r!(2-p+r)} \right] \\
&= z^{p-2} \cos\left[\frac{\pi}{2}(p-2)\right] \Gamma(2-p) - k_0^{2-p} \sum_{r=0}^{\infty} \frac{(-1)^r (k_0 z)^{2r}}{(2r)!(2-p+2r)}. \tag{A.12}
\end{aligned}$$

Using Equations A.12 and A.2 in Equation A.1 and substituting $\rho |\cos(\theta - \phi)| = z$ gives

$$\begin{aligned}
C_p(\rho, \phi) &= 1 + \frac{(p-2)}{\frac{\pi}{3}\theta_0 \operatorname{erf}\left(\frac{\sqrt{3}\pi}{2\theta_0}\right)} \cos\left[\frac{\pi}{2}(p-2)\right] \Gamma(2-p) (k_0 \rho)^{p-2} I_1(p-2, \phi) \\
&\quad - \frac{(p-2)}{\frac{\pi}{3}\theta_0 \operatorname{erf}\left(\frac{\sqrt{3}\pi}{2\theta_0}\right)} \sum_{r=1}^{\infty} \frac{(-1)^r (k_0 \rho)^{2r}}{(2r)!(2-p+2r)} I_1(2r, \phi) \tag{A.13}
\end{aligned}$$

where

$$I_1(\nu, \phi) = \int_{\theta_{Az} - \frac{\pi}{2}}^{\theta_{Az} + \frac{\pi}{2}} d\theta |\cos(\theta - \phi)|^\nu e^{-3\left(\frac{\theta - \theta_{Az}}{\theta_0}\right)^2}. \tag{A.14}$$

An equivalent form for $C_p(\rho, \phi)$ is obtained by Johnson (Johnson, 1994) by expanding Equation A.1 in terms of a generalized hypergeometric function.

The derivation for $p = 4$ must be handled separately because Equation A.10 is not valid for a equal to a negative integer. Note that $p = 4$ corresponds to $a = -2$. To find a result useful when $p = 4$, first consider the expansion derived by (Arfken, 1985, p. 567) for $a = 0$:

$$\int_x^{\infty} dt t^{-1} e^{-t} = -\gamma - \ln x - \sum_{r=1}^{\infty} \frac{(-1)^r x^r}{(r)r!} \tag{A.15}$$

where γ is the Euler-Mascheroni constant ($\gamma = 0.577215664901 \dots$). Now consider the case where $a = -1$.

$$\int_x^{\infty} dt t^{-2} e^{-t} = t^{-1} e^{-t} \Big|_x^{\infty} - \int_x^{\infty} dt t^{-1} e^{-t}$$

$$\begin{aligned}
&= \frac{e^{-x}}{x} + \gamma + \ln x + \sum_{r=1}^{\infty} \frac{(-1)^r x^r}{(r)r!} \\
&= \gamma + \ln x + \sum_{r=0}^{\infty} \frac{(-1)^r x^{r-1}}{r!} + \sum_{r=2}^{\infty} \frac{(-1)^{r-1} x^{r-1}}{(r-1)(r-1)!} \\
&= \gamma + \ln x + \frac{1}{x} - 1 + \sum_{r=2}^{\infty} \frac{(-1)^{r-1} x^{r-1}}{(r-1)r!} \\
&= \gamma + \ln x + \frac{1}{x} - 1 + \sum_{r=1}^{\infty} \frac{(-1)^r x^r}{(r)(r+1)!} \tag{A.16}
\end{aligned}$$

This result can be used to find the series for $a = -2$ which corresponds to $p = 4$

$$\begin{aligned}
\int_x^{\infty} dt t^{-3} e^{-t} &= -\frac{t^{-2}}{2} e^{-t} \Big|_x^{\infty} - \frac{1}{2} \int_x^{\infty} dt t^{-2} e^{-t} \\
&= \frac{e^{-x}}{2x^2} - \frac{\gamma}{2} - \frac{1}{2} \ln x - \frac{1}{2x} + \frac{1}{2} - \frac{1}{2} \sum_{r=1}^{\infty} \frac{(-1)^r x^r}{(r)(r+1)!} \\
&= \frac{1}{2} \left(1 - \gamma - \ln x - \frac{1}{x} + \sum_{r=0}^{\infty} \frac{(-1)^r x^{r-2}}{r!} - \sum_{r=1}^{\infty} \frac{(-1)^r x^r}{(r)(r+1)!} \right) \\
&= \frac{1}{2} \left(1 - \gamma - \ln x - \frac{1}{x} + \frac{1}{x^2} - \frac{1}{x} + \frac{1}{2} \right. \\
&\quad \left. + \sum_{r=3}^{\infty} \frac{(-1)^r x^{r-2}}{r!} - \sum_{r=1}^{\infty} \frac{(-1)^r x^r}{(r)(r+1)!} \right) \\
&= \frac{1}{2} \left(\frac{3}{2} - \gamma - \ln x - \frac{2}{x} + \frac{1}{x^2} + \sum_{r=1}^{\infty} \frac{(-1)^r x^r}{(r+2)!} - \sum_{r=1}^{\infty} \frac{(-1)^r x^r}{(r)(r+1)!} \right) \\
&= \frac{1}{2} \left(\frac{3}{2} - \gamma - \ln x - \frac{2}{x} + \frac{1}{x^2} - 2 \sum_{r=1}^{\infty} \frac{(-1)^r x^r}{(r)(r+2)!} \right) \\
&= \frac{3}{4} - \frac{\gamma}{2} - \frac{1}{2} \ln x - \frac{1}{x} + \frac{1}{2x^2} - \sum_{r=1}^{\infty} \frac{(-1)^r x^r}{(r)(r+2)!} \tag{A.17}
\end{aligned}$$

Equation A.17 can be used to evaluate Equation A.5 when $p = 4$.

$$\begin{aligned}
&\frac{(-iz)^2}{2} \int_{-izk_0}^{\infty} dt t^{-3} e^{-t} + \frac{(iz)^2}{2} \int_{izk_0}^{\infty} dt t^{-3} e^{-t} \\
&= \frac{(-iz)^2}{2} \left[\frac{3}{4} - \frac{\gamma}{2} - \frac{1}{2} \ln(-izk_0) - \frac{1}{-izk_0} + \frac{1}{2(-izk_0)^2} - \sum_{r=1}^{\infty} \frac{(-1)^r (-izk_0)^r}{(r)(r+2)!} \right] \\
&\quad + \frac{(iz)^2}{2} \left[\frac{3}{4} - \frac{\gamma}{2} - \frac{1}{2} \ln(izk_0) - \frac{1}{izk_0} + \frac{1}{2(izk_0)^2} - \sum_{r=1}^{\infty} \frac{(-1)^r (izk_0)^r}{(r)(r+2)!} \right] \\
&= \frac{1}{2k_0^2} + z^2 \left[\frac{\gamma}{2} - \frac{3}{4} + \frac{1}{2} \ln(k_0 z) + \sum_{r=1}^{\infty} \frac{(-1)^r (k_0 z)^{2r}}{(2r)(2r+2)!} \right] \tag{A.18}
\end{aligned}$$

Using Equations A.18 and A.2 in Equation A.1 and substituting $\rho|\cos(\theta - \phi)| = z$ gives the correlation coefficient for $p = 4$.

$$\begin{aligned}
C_4(\rho, \phi) = 1 &+ \frac{(k_0\rho)^2}{\frac{\pi}{3}\theta_0\text{erf}(\frac{\sqrt{3}\pi}{2\theta_0})} I_2(\rho, \phi) + (\gamma - \frac{3}{2}) \frac{(k_0\rho)^2}{\frac{\pi}{3}\theta_0\text{erf}(\frac{\sqrt{3}\pi}{2\theta_0})} I_1(2, \phi) \\
&- \frac{1}{\frac{\pi}{3}\theta_0\text{erf}(\frac{\sqrt{3}\pi}{2\theta_0})} \sum_{r=2}^{\infty} \frac{(-1)^r (k_0\rho)^{2r}}{(2r-2)(2r)!} I_1(2r, \phi) \quad (\text{A.19})
\end{aligned}$$

where $I_1(\nu, \phi)$ is given by Equation A.14, and $I_2(\rho, \phi)$ is given by

$$I_2(\rho, \phi) = \int_{\theta_{Az}-\frac{\pi}{2}}^{\theta_{Az}+\frac{\pi}{2}} d\theta \cos^2(\theta - \phi) \ln(k_0\rho|\cos[\theta - \phi]|) \exp \left[-3 \left(\frac{\theta - \theta_{Az}}{\theta_0} \right)^2 \right]. \quad (\text{A.20})$$

Appendix B

DERIVATION OF BACKSCATTER ASSUMING HORIZONTAL POLARIZATION

The derivation of the backscatter assuming a horizontally polarized source is now considered. The beginning of the derivation is identical to that for the vertically polarized case, the first variation being with the equation for the incident magnetic field (Equation 2.17). Since the source is now assumed horizontally polarized, the incident electric field is given by

$$\vec{E}_i(\vec{r}') = \hat{y} E_0 e^{i\vec{k} \cdot \vec{r}'} = \hat{y} \frac{E_0}{\eta_0} e^{ik(x' \sin \theta_i - z' \cos \theta_i)}. \quad (\text{B.1})$$

The incident magnetic field can be found by Faraday's law and is given by

$$\vec{H}_i(\vec{r}') = \frac{E_0}{\eta_0} (\hat{x} \cos \theta_i + \hat{z} \sin \theta_i) e^{ik(x' \sin \theta_i - z' \cos \theta_i)}. \quad (\text{B.2})$$

Recalling that the normal vector to the surface is given by (Equation 2.16)

$$\hat{n} = \frac{\hat{z} - \frac{\partial \eta}{\partial x'} \hat{x} - \frac{\partial \eta}{\partial y'} \hat{y}}{\left[1 + \left(\frac{\partial \eta}{\partial x'}\right)^2 + \left(\frac{\partial \eta}{\partial y'}\right)^2\right]^{\frac{1}{2}}}, \quad (\text{B.3})$$

the surface current can be found using

$$\vec{J}_s(\vec{r}') = 2\hat{n} \times \vec{H}_i(\vec{r}') \big|_{z'=\eta(x',y')}. \quad (\text{B.4})$$

As in the vertically polarized case, Equation B.4 models the current on the surface as the current that would be present on a tangent plane at each point. The tangent plane approximation requires that the radius of curvature on the surface be large when compared with an electromagnetic wavelength, which is valid for most surfaces of interest. As will be seen, the tangent plane approximation also does not account for any difference between horizontal and vertical polarizations.

Substituting Equations B.2 and B.3 into Equation B.4 gives

$$\begin{aligned} \vec{J}_s(\vec{r}') = & \left[-\hat{x} \frac{\partial \eta}{\partial y'} \sin \theta_i + \hat{y} \left(\cos \theta_i + \frac{\partial \eta}{\partial x'} \sin \theta_i \right) + \hat{z} \frac{\partial \eta}{\partial y'} \cos \theta_i \right] \\ & \frac{2E_0 e^{ik(x' \sin \theta_i - \eta(x',y') \cos \theta_i)}}{\eta_0 \left[1 + \left(\frac{\partial \eta}{\partial x'}\right)^2 + \left(\frac{\partial \eta}{\partial y'}\right)^2\right]^{\frac{1}{2}}} \delta[z' - \eta(x',y')]. \end{aligned} \quad (\text{B.5})$$

The surface current found in Equation B.5 can now be substituted into Green's theorem (Equation 2.10). This yields

$$\vec{E}_s(\vec{r}) = \frac{-ikE_0}{2\pi r} e^{ikr} \int_{-\frac{L}{2}}^{\frac{L}{2}} dy' \int_{-\frac{L}{2}}^{\frac{L}{2}} dx' \int_{-\infty}^{\infty} dz' \delta[z' - \eta(x'y')] \frac{\hat{y}(\cos \theta_i + \frac{\partial \eta}{\partial x'} \sin \theta_i)}{\left[1 + \left(\frac{\partial \eta}{\partial x'}\right)^2 + \left(\frac{\partial \eta}{\partial y'}\right)^2\right]^{\frac{1}{2}}} e^{i2k(x' \sin \theta_i - z' \cos \theta_i)}. \quad (\text{B.6})$$

Integrating the delta function gives

$$\vec{E}_s(\vec{r}) = \frac{-ikE_0}{2\pi r} e^{ikr} \int_{-\frac{L}{2}}^{\frac{L}{2}} dy' \int_{-\frac{L}{2}}^{\frac{L}{2}} dx' \hat{y}(\cos \theta_i + \frac{\partial \eta}{\partial x'} \sin \theta_i) \frac{\left[1 + \left(\frac{\partial \eta}{\partial x'}\right)^2 + \left(\frac{\partial \eta}{\partial y'}\right)^2 + \left(\frac{\partial \eta}{\partial x'}\right)^2 \left(\frac{\partial \eta}{\partial y'}\right)^2\right]^{\frac{1}{2}}}{\left[1 + \left(\frac{\partial \eta}{\partial x'}\right)^2 + \left(\frac{\partial \eta}{\partial y'}\right)^2\right]^{\frac{1}{2}}} e^{i2k(x' \sin \theta_i - \eta(x',y') \cos \theta_i)}. \quad (\text{B.7})$$

As in the vertically polarized case, $\left(\frac{\partial \eta}{\partial x'}\right)^2 \left(\frac{\partial \eta}{\partial y'}\right)^2$ and $\frac{\partial \eta}{\partial x'} \sin \theta_i$ are negligible. Thus, Equation B.7 simplifies to

$$\vec{E}_s(\vec{r}) = \frac{-ik \cos \theta_i E_0}{2\pi r} e^{ikr} \hat{y} \int_{-\frac{L}{2}}^{\frac{L}{2}} dy' \int_{-\frac{L}{2}}^{\frac{L}{2}} dx' e^{i2k(x' \sin \theta_i - \eta(x',y') \cos \theta_i)}. \quad (\text{B.8})$$

Since an expression for $|\vec{E}_s(\vec{r})|^2$ is desired, Equation B.8 is expanded, giving

$$|\vec{E}_s(\vec{r})|^2 = \frac{k^2 \cos^2 \theta_i E_0^2}{4\pi^2 r^2} \int_{-\frac{L}{2}}^{\frac{L}{2}} dy' \int_{-\frac{L}{2}}^{\frac{L}{2}} dx' \int_{-\frac{L}{2}}^{\frac{L}{2}} dy \int_{-\frac{L}{2}}^{\frac{L}{2}} dx e^{i2k[(x'-x) \sin \theta_i + (\eta(x,y) - \eta(x',y')) \cos \theta_i]}. \quad (\text{B.9})$$

This expression is identical to Equation 2.22, which was derived assuming vertical polarization. Thus, when Equation B.9 is substituted into Equation 2.23, the same expression for the backscatter integral (Equation 2.27) results. Thus, when using the tangent plane approximation, no dependence of the backscatter on polarization is predicted.

MEAN AND FLUCTUATING FIELDS

It is sometimes insightful to separate the scattered electromagnetic fields into a mean field and a fluctuating field. The mean field is denoted $\vec{E}_{sm}(\vec{r})$; the fluctuating field is represented by $\vec{\mathcal{E}}_{sf}(\vec{r})$, and, as in previous derivations, the total scattered field is denoted $\vec{E}_s(\vec{r})$. The definitions of $\vec{E}_{sm}(\vec{r})$ and $\vec{\mathcal{E}}_{sf}(\vec{r})$ are as follows (recall that angle brackets denote statistical expectation):

$$\vec{E}_{sm}(\vec{r}) = \langle \vec{E}_s(\vec{r}) \rangle \quad (\text{C.1})$$

$$\vec{\mathcal{E}}_{sf}(\vec{r}) = \vec{E}_s(\vec{r}) - \vec{E}_{sm}(\vec{r}) \quad (\text{C.2})$$

Thus, $\vec{E}_s(\vec{r})$ is the sum of the two parts,

$$\vec{E}_s(\vec{r}) = \vec{E}_{sm}(\vec{r}) + \vec{\mathcal{E}}_{sf}(\vec{r}). \quad (\text{C.3})$$

Note that a consequence of these definitions is $\langle \vec{\mathcal{E}}_{sf}(\vec{r}) \rangle = 0$.

To find the normalized radar cross-section, $\langle |\vec{E}_s(\vec{r})|^2 \rangle$ needs to be evaluated. It follows from the definitions of $\vec{E}_{sm}(\vec{r})$ and $\vec{\mathcal{E}}_{sf}(\vec{r})$ that

$$\begin{aligned} \langle |\vec{E}_s(\vec{r})|^2 \rangle &= \langle |\vec{E}_{sm}(\vec{r}) + \vec{\mathcal{E}}_{sf}(\vec{r})|^2 \rangle \\ &= \langle [|\vec{E}_{sm}(\vec{r}) + \vec{\mathcal{E}}_{sf}(\vec{r})|][|\vec{E}_{sm}(\vec{r}) + \vec{\mathcal{E}}_{sf}(\vec{r})|^*] \rangle \\ &= \langle |\vec{E}_{sm}(\vec{r})|^2 \rangle + \langle |\vec{\mathcal{E}}_{sf}(\vec{r})|^2 \rangle + \langle \vec{E}_{sm}(\vec{r})\vec{\mathcal{E}}_{sf}(\vec{r})^* \rangle + \langle \vec{E}_{sm}(\vec{r})^*\vec{\mathcal{E}}_{sf}(\vec{r}) \rangle \\ &= |\vec{E}_{sm}(\vec{r})|^2 + \langle |\vec{\mathcal{E}}_{sf}(\vec{r})|^2 \rangle + \vec{E}_{sm}(\vec{r})\langle \vec{\mathcal{E}}_{sf}(\vec{r})^* \rangle + \vec{E}_{sm}(\vec{r})^*\langle \vec{\mathcal{E}}_{sf}(\vec{r}) \rangle \\ &= |\vec{E}_{sm}(\vec{r})|^2 + \langle |\vec{\mathcal{E}}_{sf}(\vec{r})|^2 \rangle. \end{aligned} \quad (\text{C.4})$$

Recalling the definition of the normalized radar cross-section (see Equation 2.23),

$$\begin{aligned} \sigma^\circ &= \frac{4\pi r^2}{L^2} \left\langle \frac{|\vec{E}_s(\vec{r})|^2}{E_0^2} \right\rangle \\ &= \frac{4\pi r^2}{L^2 E_0^2} |\vec{E}_{sm}(\vec{r})|^2 + \frac{4\pi r^2}{L^2 E_0^2} \langle |\vec{\mathcal{E}}_{sf}(\vec{r})|^2 \rangle \\ &\equiv \sigma_m^\circ + \sigma_f^\circ \end{aligned} \quad (\text{C.5})$$

To evaluate the terms in Equation C.5, define

$$I = \int_{-\frac{L}{2}}^{\frac{L}{2}} dy' \int_{-\frac{L}{2}}^{\frac{L}{2}} dx' e^{i2k(x' \sin \theta_i - \eta(x', y') \cos \theta_i)}. \quad (\text{C.6})$$

With this definition,

$$\langle |\vec{E}_s(\vec{r})|^2 \rangle = \frac{k^2 \cos^2 \theta_i E_0^2}{4\pi^2 r^2} \langle II^* \rangle \quad (\text{C.7})$$

(see Equations 2.21, 2.22, B.8, and B.9). Thus,

$$\sigma^o = \frac{k^2 \cos^2 \theta_i}{\pi L^2} \langle II^* \rangle. \quad (\text{C.8})$$

Note that evaluating $\langle II^* \rangle$ leads to Equation 2.27, the backscatter integral.

Next, note that by definition, $\vec{E}_{sm}(\vec{r}) = \langle \vec{E}_s(\vec{r}) \rangle$. It follows that,

$$|\vec{E}_{sm}(\vec{r})|^2 = |\langle \vec{E}_s(\vec{r}) \rangle|^2 = \frac{k^2 \cos^2 \theta_i E_0^2}{4\pi^2 r^2} |\langle I \rangle|^2 \quad (\text{C.9})$$

Thus, evaluating $|\vec{E}_{sm}(\vec{r})|^2$ becomes a problem of evaluating $|\langle I \rangle|^2$. $|\langle I \rangle|^2$ can be written

$$|\langle I \rangle|^2 = \left| \int_{-\frac{L}{2}}^{\frac{L}{2}} dx' e^{i2kx' \sin \theta_i} \int_{-\frac{L}{2}}^{\frac{L}{2}} dy' \langle e^{-i2k\eta(x', y') \cos \theta_i} \rangle \right|^2. \quad (\text{C.10})$$

Since $\eta(x', y')$ is a Gaussian random variable with zero mean and variance σ^2 , its density is known. Thus, $\langle e^{-i2k\eta(x', y') \cos \theta_i} \rangle$ can be evaluated in terms of the definition of a statistical expectation.

$$\begin{aligned} \langle e^{-i2k\eta(x', y') \cos \theta_i} \rangle &= \int_{-\infty}^{\infty} dz e^{-i2kz \cos \theta_i} f_{\eta}(z) \\ &= e^{-2\sigma^2 k^2 \cos^2 \theta_i} \end{aligned} \quad (\text{C.11})$$

Substituting back into Equation C.10,

$$\begin{aligned} |\langle I \rangle|^2 &= e^{-4\sigma^2 k^2 \cos^2 \theta_i} L^2 \left| \int_{-\frac{L}{2}}^{\frac{L}{2}} dx' e^{i2kx' \sin \theta_i} \right|^2 \\ &= e^{-4\sigma^2 k^2 \cos^2 \theta_i} L^4 \text{sinc}^2 \left(\frac{kL \sin \theta_i}{\pi} \right) \end{aligned} \quad (\text{C.12})$$

where $\text{sinc}(x) \equiv \frac{\sin \pi x}{\pi x}$. Using Equation C.12 in Equation C.9 gives

$$|\vec{E}_{sm}(\vec{r})|^2 = \frac{k^2 L^4 \cos^2 \theta_i E_0^2}{4\pi^2 r^2} e^{-4\sigma^2 k^2 \cos^2 \theta_i} \text{sinc}^2 \left(\frac{kL \sin \theta_i}{\pi} \right). \quad (\text{C.13})$$

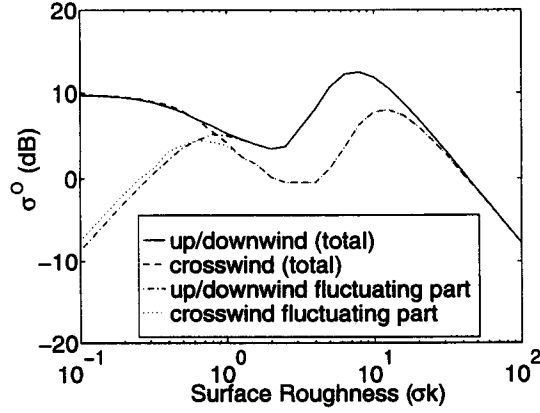


Figure C.1: Fluctuating backscatter compared to total backscatter. Notice that when the roughness is small, the backscatter contains a large mean part. When the roughness is large, the fluctuating part dominates the backscatter. The plots were generated with $p = 4.0$, $k_0 = 1.5m^{-1}$, $\theta_0 = 90^\circ$, $\theta_i = 10^\circ$, and $f = 10GHz$ ($k = 209m^{-1}$). Up/downwind corresponds to $\theta_{Az} = 0^\circ$, and crosswind corresponds to $\theta_{Az} = 90^\circ$

It then follows that

$$\sigma_m^\circ = \frac{(kL)^2 \cos^2 \theta_i}{\pi} e^{-4(\sigma k)^2 \cos^2 \theta_i} \text{sinc}^2 \left(\frac{(kL) \sin \theta_i}{\pi} \right). \quad (C.14)$$

Putting it all together, the scattered electromagnetic fields, and hence σ° , can be expressed in terms of a mean part and a fluctuating part. Hence, σ° can be written $\sigma^\circ = \sigma_m^\circ + \sigma_f^\circ$. σ° is given by $\frac{k^2 \cos^2 \theta_i}{\pi L^2} \langle II^* \rangle$ where I is as defined in Equation C.6. Pursing the derivation of $\langle II^* \rangle$ leads to the backscatter integral. σ_m° is proportional to the mean part of the backscatter, and can be expressed as

$$\sigma_m^\circ = \frac{(kL)^2 \cos^2 \theta_i}{\pi} e^{-4(\sigma k)^2 \cos^2 \theta_i} \text{sinc}^2 \left(\frac{(kL) \sin \theta_i}{\pi} \right). \quad (C.15)$$

σ_f° can then be found from $\sigma_f^\circ = \sigma^\circ - \sigma_m^\circ$. σ_m° can be interpreted as being proportional to the coherent scattered power, and σ_f° as being proportional to the incoherent scattered power. Figure C.1 compares the total backscatter to the fluctuating part of the backscatter. Intuitively, a smooth surface scatters most of the power in one direction; hence, for small roughnesses there is a large mean (coherent) part present in the backscatter. A rough surface scatters power in many directions; for large roughnesses, the backscatter is dominated by the fluctuating (incoherent) part.

AZIMUTH MODULATION OF THE RADAR
BACKSCATTER AT NEAR-NORMAL
INCIDENCE

Andrew D. Greenwood


Department of Electrical and Computer Engineering

M. S. Degree, June 7, 1995

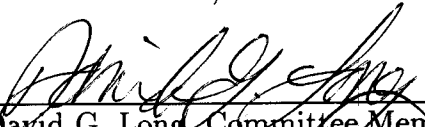
ABSTRACT

A two dimensional surface model is used to derive the near-normal radar backscatter from the ocean surface. The model assumes Gaussian surface statistics, and a k_w^{-p} power spectral density. The directional dependence on the spectrum is modeled by a Gaussian function. The backscatter is derived using Green's theorem and a physical optics approach. The derived backscatter predicts azimuth modulation at near-normal incidence (0 to 10dB at 10° incidence). The modulation is characterized and explained physically in terms of the orientation of surface facets in different azimuth directions. The effects of surface and radar parameters are discussed. The theoretical results are compared to radar data from the BYU YSCAT94 radar experiment. The theory correctly predicts a cosine-like shape of the normalized radar cross-section plotted as a function of azimuth angle. It also predicts correctly that the modulation will decrease when the surface roughness increases. However, its predictions of the modulation as a function of frequency are limited by the assumptions in the surface model. A surface model that includes a directional dependence on wave number may correct the frequency predictions.

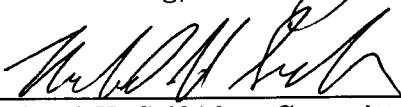
COMMITTEE APPROVAL:



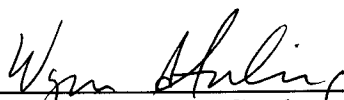
David V. Arnold, Committee Chairman



David G. Long, Committee Member



Richard H. Selfridge, Committee Member



Wynn C. Stirling, Graduate Coordinator